HHS Public Access

Author manuscript

Biomed Pharmacother. Author manuscript; available in PMC 2026 February 11.

Published in final edited form as:

Biomed Pharmacother. 2026 January ; 194: 118915. doi:10.1016/j.biopha.2025.118915.

Establishment of a human inner ear model reveals that gentamicin C2b is substantially less ototoxic than clinical gentamicin

Minjin Jeong[a], **Hiroaki Mohri**[a,1], **Dongjun Han**[a,1], **Masaharu Sakagami**[a], **Konstantina M. Stankovic**[a,b,c,*]

[a]Department of Otolaryngology–Head and Neck Surgery, Stanford University School of Medicine, 801 Welch Rd., Stanford, CA 94304, USA

[b]Department of Neurosurgery, Stanford University School of Medicine, 300 Pasteur Dr., Stanford, CA 94304, USA

[c]Wu Tsai Neurosciences Institute, Stanford University, 288 Campus Dr., Stanford, CA 94304, USA

Abstract

Clinically used gentamicin, a widely used aminoglycoside antibiotic, is a mixture of 5 major subtypes with potentially differential contributions to the drug's known ototoxicity. The gentamicin subtype C2b has been previously associated with reduced ototoxicity in animal models in vitro, but its effects in humans remain uncertain due to the lack of appropriate in vitro models of the human inner ear. To address this gap, we generated otic progenitor cells (OPCs) from human induced pluripotent stem cells and used transcriptomic and immuno-cytochemical analyses to confirm their otic lineage identity and validate their relevance as a model for ototoxicity studies. We then compared the effects of gentamicin C2b and clinical gentamicin on cell viability and cytotoxicity in human OPCs. In parallel, we examined auditory function in mice following exposure to each formulation using auditory brainstem response and distortion product otoacoustic emissions. Gentamicin C2b exposure resulted in substantially lower cytotoxicity—via reduced mitochondria-dependent apoptosis—and higher cell viability in human OPCs, as well as dramatically attenuated hearing loss across all frequencies in mice. Together, these findings indicate that gentamicin C2b has reduced ototoxicity compared to clinically used preparations, supporting the need for further investigations in clinical settings.

*Corresponding author at: Department of Otolaryngology–Head and Neck Surgery, Stanford University School of Medicine, 801 Welch Rd., Stanford, CA 94304, USA. kstankovic@stanford.edu (K.M. Stankovic).

[1]Equally contributed

CRediT authorship contribution statement

Hiroaki Mohri: Writing – review & editing, Writing – original draft, Visualization, Validation, Resources, Methodology, Formal analysis, Data curation, Conceptualization. **Minjin Jeong:** Writing – review & editing, Writing – original draft, Visualization, Validation, Resources, Project administration, Methodology, Investigation, Formal analysis, Data curation, Conceptualization. **Masaharu Sakagami:** Visualization, Validation, Methodology, Formal analysis, Data curation. **Dongjun Han:** Writing – review & editing, Visualization, Software, Methodology, Formal analysis, Data curation. **Konstantina Stankovic:** Writing – review & editing, Supervision, Resources, Methodology, Funding acquisition, Conceptualization.

Declaration of Competing Interest

The authors declare that they have no known competing financial interests or personal relationships that could have appeared to influence the work reported in this paper.

Keywords

Aminoglycoside antibiotic; Gentamicin; Gentamicin C2b; Human induced pluripotent stem cells; Otic progenitor cells; Ototoxicity; Mouse auditory brainstem evoked response

1. Introduction

Gentamicin, a broad-spectrum aminoglycoside antibiotic derived from Micromonospora purpurea [1], is used worldwide to treat serious, particularly gram-negative, bacterial infections [2]. Due to its efficacy [3,4], affordability, and wide availability, it has been classified as an essential medicine by the World Health Organization since 1977 [5]. Despite its medical importance, gentamicin is associated with adverse effects such as nephrotoxicity and ototoxicity, the latter of which can cause permanent sensorineural hearing loss (SNHL) [6–8]. The incidence of gentamicin-induced ototoxicity varies across populations and administration protocols, with reported rates as high as 25 % [9,10], although the true rate may be higher in developing nations where gentamicin is more commonly used and available without prescription.

Aminoglycosides like gentamicin exert their antibacterial effects by entering bacterial cells via oxygen-dependent active transport and binding to ribosomes, thereby disrupting mRNA translation and inducing cell death [11,12]. Unfortunately, these antibiotics also enter the sensory cells of the cochlea—the hair cells—via mechanotransduction channels [13], transient receptor potential (TRP) channels [14], and ATP channels [15], or through endocytosis [16], inducing toxic intracellular effects. Once inside hair cells, gentamicin binds to ribosomes, disrupts protein synthesis, and induces oxidative stress, ultimately triggering apoptosis through primarily mitochondria-dependent pathways [13–16]. As a result, ototoxicity is a major dose-limiting factor in the clinical use of gentamicin [17], driving the need for strategies to protect the inner ear without compromising the antibacterial efficacy of this globally important medication.

Currently used clinical preparations of gentamicin consist of a mixture of the C complexes C1, C1a, C2, C2a, and C2b (≥90 %), along with minor components and impurities [18]. These C components have varying methylation patterns determined by specific methyltransferases [19], which can influence their binding affinities, antibacterial activity, and importantly, their interactions with mitochondrial ribosomes that dictate their toxicity profiles [20,21]. Among the major components, gentamicin C2b (also known as micronomicin, XK-62–2, sagamicin, or KW-1062 [22]) has demonstrated reduced ototoxicity in animal models. Early studies in guinea pigs suggested that the ototoxicity of gentamicin C2b is approximately four times lower than that of clinical gentamicin, as measured by pinna reflex tests [23], and the degree of hair cell loss was mild [24]. A more recent study demonstrated that gentamicin C2b induced significantly less ototoxicity in rat cochlear hair cell explants compared to hospital-grade gentamicin, while retaining comparable antimicrobial activity [25]. However, despite these encouraging findings, the impact of gentamicin C2b on auditory function in vivo, particularly as assessed by objective measures such as auditory brainstem response (ABR) or distortion product otoacoustic

emissions (DPOAEs), remains largely unknown. Likewise, its effects on human inner ear cells in vitro have not yet been systematically examined.

Although animal models are indispensable for auditory research, the resultant findings often fail to fully translate to humans due to cross-species differences in physiology and genetics. For example, animal models are unable to recapitulate all genes and pathways involved in human hereditary hearing loss [26]. Moreover, mice display limited hearing loss following systemic gentamicin delivery, as is used in clinical practice, and require intracochlear infusion to mimic the ototoxic effects occurring in humans [27]. Thus, a more balanced approach to provide a broader understanding of drug-induced ototoxicity is to integrate the results from animal models with human in vitro models that can more accurately mimic human inner ear cell dynamics.

Recent advances in human induced pluripotent stem cell (hiPSC) technology have opened new avenues for developing in vitro models of the human inner ear. Notably, otic progenitor cells (OPCs) derived from hiPSCs [28] have been applied in studies on viral-induced hearing loss [29,30] and oxidative stress-induced damage models [31]. These studies highlight the potential of OPCs as a human inner ear model, although their comprehensive characterization—such as determining their comparable inner ear developmental stage in vivo or assessing the proportion of inner ear-related cells within these populations—remains incomplete.

To this end, we characterized hiPSC-derived OPCs using bulk and single-cell RNA sequencing (scRNA-seq), alongside immunocytochemistry, to support their relevance and reliability as a human inner ear model system for aminoglycoside toxicity testing. Following validation of the platform, we used OPCs to investigate the differential ototoxic effects of exposure to gentamicin or its C2b subtype by comparing cell viability, cytotoxicity, mitochondrial activity, and apoptosis. In parallel, we examined the impact of the two gentamicin preparations on the hearing thresholds of mice to assess their impact on mammalian auditory function in vivo.

2. Materials and methods

2.1. hiPSCs culture and OPC differentiation

hiPSC lines SK8-A [29], and UCSD112i-2–11 (UCSD), purchased from WiCell, on Geltrex (Gibco, A1413302) were cultured in mTeSR Plus medium (StemCell Technologies, 100–0276). hiPSC colonies were detached using ReLeSR (StemCell Technologies, 05872) and transferred onto Geltrex-coated plates. hiPSCs were maintained under mTeSR Plus medium and used up to passage number 50.

We used a previously published protocol for the differentiation of hiPSCs into OPCs using a monolayer culture system [29]. Briefly, un-differentiated hiPSC lines SK8-A and UCSD were dissociated with ReL-eSR and seeded at 30,000 cells/cm^2 onto laminin-coated plates (R&D Systems, 3401–010–02) and cultured in DMEM/F12 (Gibco, 11330032) supplemented with 1 × N2 (1 % (v/v) final concentration, Gibco, 17502048), 1 × B27 (2 % (v/v) final concentration, Gibco, 17504044), 50 ng/mL FGF-3 (R&D Systems, 1206-F3),

and 50 ng/mL FGF-10 (R&D Systems, 345-FG). The medium was replaced on day 0 and changed every other day. The concentration of Y-27632 (TOCRIS, 1254) was maintained at 10 μM throughout days 0–3. On day 14, the cells were transferred onto growth factor reduced Matrigel (Corning, 356230)-coated plates at 80,000 cells/cm^2 and cultured in DMEM/F12 supplemented with 1 × N2, 1 × B27, 5 μM Dibenzazepine (DBZ; TOC-RIS, 4489), and 10 μM Y-27632. The medium without Y-27632 was replaced every other day from day 15 to day 20.

2.2. RNA sequencing

2.2.1. RNA isolation and analytic pipeline for bulk RNA sequencing: hiPSCs (SK8-A and UCSD; n = 3 per line) were harvested at approximately 80 % confluency and total RNA was extracted. Additionally, day 20 OPCs (n = 3 per line) derived from both hiPSC lines were collected for RNA isolation. The quality of RNA samples was assessed, ensuring a purity ratio (A260/280) between 1.8 and 2.2 and an RNA integrity number above 6. The RNA samples were subjected to poly (A) + selection, cDNA synthesis, and sequencing using Illumina Nova-Seq in GENEWIZ (https://www.genewiz.com/), resulting in 350 million raw paired-end reads per lane.

Subsequent data processing was performed on Ubuntu WSL (v24.04.1 LTS) using a custom Python-based pipeline. Adapter trimming and quality filtering were conducted using Trimmomatic (v0.40). Cleaned reads were aligned to the human reference genome (GRCh38. p14) using HISAT2 (v2.2.1). Gene-level quantification was carried out with FeatureCounts from the Subread package (v2.1.1). The resulting raw count matrix was used for downstream analysis. Count data were analyzed in R (v4.5.0) within the RStudio environment (v2025.05.0 +496). Differential expression analysis was performed using DESeq2 (v1.48.1), with log-fold change shrinkage applied using apeglm (v1.30.0). Gene annotation was facilitated by AnnotationDbi (v1.70.1) and clusterProfiler (v4.16.0). Principal component analysis (PCA) was carried out using PCATools (v2.20.0). All graphical outputs were generated using functions from the aforementioned software and R packages, including ComplexHeatmap (v2.24.0) and ggplot2 (v3.5.2).

2.2.2. Gene set enrichment analysis: Differentially expressed genes with |log2(fold-change)| > 1 in hiPSCs compared to OPCs were used as input for gene set enrichment analysis using Cytoscape with the Bingo plugin. The most recent Gene Ontology (GO) file “go-basic.obo” was downloaded from the Gene Ontology Consortium website (http://geneontology.org/) instead of using Bingo’s default ontologies. Significant GO terms (adjusted $p < 0.05$) were used as input for Cytoscape’s Enrichment Map plugin to generate a network.

2.2.3. Dissociation of OPCs for scRNA-seq: To prepare a single-cell suspension for scRNA-seq, OPCs differentiated from hiPSCs (SK8-A and UCSD) were collected from randomly selected wells at day 14 (n = 3) and day 20 (n = 3) and pooled. Cells were incubated with TrypLE Select in a 37°C incubator for about 2 min, until detachment was observed at the colony edges. TrypLE was then removed, and the cells were gently resuspended in DMEM/F12 supplemented with 10 % fetal bovine serum (Gibco, 26140079)

using a P1000 pipette until no visible aggregates remained. The cell suspension was passed through a 100 μm cell strainer to remove residual clumps, then resuspended in 1X phosphate-buffered saline (PBS; Gibco, 14190144) containing 0.04 % bovine serum albumin (BSA; SIGMA, A8412). Cell viability was assessed using a hemocytometer and confirmed with a BioRad TC20 automated cell counter. Final cell suspensions were adjusted to 1000 cells/μL with > 80 % cell viability.

2.2.4. scRNA-seq cDNA library preparation and sequencing: Single-cell 3′ RNA-seq was performed using the Chromium Single Cell system (10X Genomics) and sequenced on a NexSeq 2000 (Illumina). Dissociated cells were added to a single-cell master mix targeting 10,000 cells, following the Chromium Single Cell 3′ v3 protocol (10X Genomics, G000183, Rev C). Along with the single-cell gel beads and oil partitioned in separate wells of a Single Cell B Chip, the single-cell reaction mixture was loaded onto the Chromium Controller for Gel Bead-in-Emulsion generation and barcoding. This was followed by cDNA synthesis and library construction. At each step, cDNA and library quality were assessed using a TapeStation 4200. Final libraries were sequenced on an Illumina NextSeq 2000, with 28-bp plus 91-bp paired-end program, achieving a reading depth of over 30,000 reads per cell.

2.2.5. scRNA-seq data analysis: Raw sequencing data were processed using the 10X Genomics Cell Ranger 2.1.0 pipeline (http://support.10xgenomics.com/). Briefly, Cell Ranger utilizes bcl2fastq (https://support.illumina.com/) to demultiplex raw base sequence calls generated from the sequencer into sample-specific FASTQ files. These FASTQ files were then aligned to the reference genome using RNA-seq aligner STAR. The aligned reads are traced back to the individual cells, and gene expression levels were quantified based on the number of unique molecular indices (UMIs) detected in each cell. Filtered gene–cell barcode matrices were generated by Cell Ranger for downstream analysis. Cells with fewer than 200 unique genes identified and cells with higher than 7–20 % mitochondrial reads were excluded. Doublets were identified and removed using DoubletFinder [32] with standard parameters, assuming a predicted doublet rate of 4.6–5.4 % based on the number of cells captured.

Following quality control, gene expression levels for each cell were normalized by the total UMI count per cell and scaled by a scaling factor of 10,000. Log-transformed data were then analyzed using Seurat (v.4.0.4–5.0.0) for cell clustering, applying PCA on highly variable genes. Cell clusters were visualized using uniform manifold approximation projection (UMAP), which preserves the global structure of the data. The gene markers for each cluster were identified through differential expression analysis by comparing cells in the cluster to all other cells. Cell cluster identities were manually defined with the cluster-specific marker genes. Data visualization was conducted using the ggplot2 package. Dot plots and feature plots were generated to illustrate specific gene expressions across clusters. Cell-cell communication analysis was performed using the CellChat package [33] with default parameters applied to intercellular signaling networks.

2.3. Cell immunocytochemistry

To assess gentamicin uptake, OPCs were incubated with 3 μM Texas Red-conjugated gentamicin-conjugated (GTTR) for 24 h prior to imaging. For mitochondria labeling, cells were treated with 100 nM Mito-Tracker (Cell Signaling Technology, 9082) at 37°C for 30 min. Following incubation, cells were processed for immunostaining.

Cultured cells were washed 3 times with PBS and fixed in 4 % paraformaldehyde (PFA; Thermo Fisher Scientific, AAJ19943K2) at room temperature for 10 min. Cells were permeabilized by washing 3 times with PBS, followed by incubation in PBST (0.1 % Triton X-100 in 1 × PBS) at room temperature for 10 min. To block nonspecific binding, cells were incubated in 5 % goat serum (Gibco, PCN5000) or 5 % normal horse serum (Abcam, ab7484) in PBST for 1 h at room temperature. Subsequently, cells were incubated overnight at 4 °C with the following primary antibodies diluted in 1 % BSA in PBST: rabbit polyclonal IgG EPCAM (EpigenTek, A68759; 1:200), mouse monoclonal IgG1 FBXO2 (Santa Cruz, sc-398111; 1:250), rabbit monoclonal GATA3 (Cell Signaling Technology, 5852; 1:800), goat polyclonal IgG PROX1 (R&D systems, AF2727; 1:20), and mouse monoclonal cytochrome c (Cell Signaling Technology, 12963; 1:300).

The next day, cells were washed 3 times with PBS and incubated with the following secondary antibodies diluted in 1 % BSA in PBST: chicken anti-goat IgG 488 (Invitrogen, A21467; 1:500), goat anti-rabbit IgG 488 (Invitrogen, A11008; 1:1000), goat anti-mouse IgG1 (Invitrogen, A21124; 1:2000), or donkey anti-rabbit IgG (Invitrogen, A10042; 1:500). Nuclei were stained with 0.1 μg/mL DAPI (Cell Signaling Technology, 4083) and samples were mounted using Vectashield (Vector Laboratories, H1000). Imaging was performed using a ZEISS LSM 880 confocal microscope.

2.4. In vitro clinical gentamicin and gentamicin C2b exposure

hiPSC-derived OPCs (day 20) were treated with gentamicin (Fresenius Kabi, 17302) and gentamicin C2b [25] at concentrations ranging from 50 μg/mL to 500 μg/mL for 24 h. For each experiment, gentamicin C2b was freshly dissolved from powder, while gentamicin provided as a liquid formulation was used directly. All working solutions were freshly prepared immediately before use to ensure consistency and stability.

2.5. In vitro assays

2.5.1. MTT assay: Twenty-four hours after gentamicin or gentamicin C2b exposure, 30 μl of MTT (3-(4,5-dimethylthiazol-2-yl)-2,5-diphenyltetrazolium bromide) stock solution (5 mg/mL; Invitrogen, M6494) was added to each well of a 24 well plate containing 300 μl of culture medium with OPCs (day 20) or hiPSCs. The cells were incubated at 37°C for 4 h, allowing the formation of insoluble purple formazan crystals. To dissolve the crystals, 330 μl of 10 % sodium dodecyl sulfate (Sigma-Aldrich, L3771) in 0.01 M HCl (Sigma-Aldrich, H9892) was added to each well, followed by overnight incubation at 37°C. Optical density was measured at 570 nm using a SpectraMax iD3 microplate reader (Molecular Devices).

2.5.2. Lactate Dehydrogenase (LDH) assay: Twenty-four hours after gentamicin and gentamicin C2b exposure, 50 μl of culture medium from each well was collected

from OPCs (day 20) or hiPSCs cultured in 24-well plates and transferred to a 96 well plate. LDH reagent (Abcam, ab102526; 50 μl) was then added to each well containing the culture medium. The detailed LDH assay protocol is available on the Abcam website (https://www.abcam.com/en-us/knowledge-center/cell-biology/ldh-assay-kit-guide-principles-and-application). Optical density was measured immediately and again after 30 min at a wavelength of 450 nm using a SpectraMax iD3 microplate reader (Molecular Devices) at 37°C, protected from light.

2.5.3. Live cell imaging: Caspase 3/7 green dye (Sartorius, 4440) was used to detect caspase 3/7 enzyme activity as an indicator of apoptosis. OPCs cultured in 24 well plates were first washed with PBS, and the culture medium was replaced with fresh medium containing 1:1000 diluted caspase 3/7 green dye along with gentamicin or gentamicin C2b. Real-time imaging was conducted every hour for 24 h at 37°C using the IncuCyte S3 live cell imaging system (Essen BioScience). For each well, 9 images at 10x magnification were captured in both phase-contrast and green fluorescence channels. Fluorescence acquisition times were set at 300 ms for the green channel. Image analysis was performed using IncuCyte®S3 Software v2018B Basic Analyzer, quantifying the number of green objects per mm^2. The analysis parameters were set as follows: Segmentation: “Surface Fit”, Threshold (GCU) “50.0000”, “Edge Split On”, Edge Sensitivity “0”; Cleanup: Hole Fill (μm^2) “0.0000”, Adjust Size (pixels) “0”; Filters: “0.0000”.

2.6. Animals procedures

2.6.1. Mice: Male CBA/J mice aged 8–10 weeks were purchased from Jackson Laboratories (Sacramento, CA, US). All animal procedures were performed in compliance with relevant laws and institutional guidelines and were approved by the Administrative Panel on Laboratory Animal Care (APLAC; number 33998) at Stanford University on 09/15/2021. All results are reported according to the ARRIVE guidelines.

2.6.2. Cochlear function testing: Cochlear function testing was performed using previously described methods [34]. In brief, mice were anesthetized via intraperitoneal injection of ketamine (120 mg/kg) and xylazine (12 mg/kg). A custom-built acoustic system consisting of two speakers (MF1, TDT, Alachua, FL, United States) and a microphone (ER-10B+, Ethymotic Research, Elk Grove Village, IL, United States) coupled to a probe tube was used to measure pressure near the mouse eardrum. DPOAEs were measured as ear canal pressure in response to two tones presented into the ear canal (f1 and f2, with f2/f1 =1.2) at half-octave steps, from f2 = 5.6–45.2 kHz, and in 5 dB intensity increments from 10 to 80 dB sound pressure level (SPL). ABR to 5-ms tone pips were measured between subdermal electrodes (placed adjacent to ipsilateral pinna, at the vertex, and near the tail), amplified 10,000 times through an amplifier (Medusa4Z, TDT, Alachua, FL, US) and filtered (0.3–3.0 kHz). For each frequency and sound level assessed, 512 responses were recorded and averaged using the BioSigRZ software run on a RZ6 Multi-I/O Processor (TDT, Alachua, FL, US). ABR waveforms stacked from lowest to highest SPL were visually inspected to define the threshold as the first level at which a repeatable waveform was visually detected. In the absence of an ABR or DPOAE response, 85 dB SPL was chosen as a threshold because it was 5 dB above the highest sound pressure level tested [35].

2.6.3. Surgical procedures: Gentamicin application to the round window of mice was performed as previously described [36]. In brief, mice were anesthetized via intraperitoneal injection of ketamine (120 mg/kg) and xylazine (12 mg/kg) and placed on a rodent heating pad. Only the left ear received treatment. The skin around the scalp was shaved and prepped. Then, a retro-auricular incision was made and the bulla uncovered. A small hole was drilled in the otic bulla and enlarged by breaking off bone with fine forceps to provide a view of the round window niche. Great care was taken to preserve the stapedial artery. A small pledget of absorbable gelatin sponge (Surgifoam, Ethicon, 1972) was soaked in saline, gentamicin (200 mg/mL in saline, Sigma-Aldrich, G-4918), or gentamicin C2b (200 mg/mL in saline, MedChemExpress, HY-B1915) and placed in the round window niche. All working solutions were freshly prepared immediately before each experiment to ensure consistency and stability. Finally, the tissue was approximated and the skin was closed with 5–0 sutures.

2.6.4. Cochlear whole mounts and immunohistochemistry: Cochlear samples from the mice were prepared as described previously [37]. A small hole was opened in the apex of the cochlea and the round and oval window membranes were punctured to allow gentle intracochlear perfusion with 4 % PFA. Cochleae were post-fixed overnight in 4 % PFA and decalcified in 0.12 M EDTA for 1 week at 4°C or for 2 days at room temperature. Whole mounts of the organ of Corti were prepared by microdissecting cochlear half turns, blocking them with 5 % goat serum and 0.3 % Triton X-100 (TX-100) in PBS for 1 h at room temperature, and incubating them overnight at 4°C with a rabbit polyclonal Myosin 7 A (Proteus Biosciences, #25–6790; 1:200) diluted in 1 % goat serum and 0.1 % TX-100. Sections were then incubated with species-appropriate secondary antibody (AlexaFluor 555 goat anti-rabbit; 1:500) for 1 h at room temperature. Stained tissues were mounted in ProLong anti-fade (Thermo Fisher Scientific) with a coverslip. Imaging was performed using a ZEISS LSM 880 confocal microscope.

2.7. Statistical analysis and reproducibility

Statistical analyses were performed using Prism 10.4, with a p-value of < 0.05 considered statistically significant for all comparisons. Unpaired *t*-tests were used to evaluate differences between control samples and drug-exposed samples, or between gentamicin- and gentamicin C2b-treated samples, in the cell viability and cytotoxicity assays. For the caspase 3/7 assay, a multiple unpaired *t*-test was used to compare gentamicin- and gentamicin C2b-exposed samples.

Representative bright-field images in Fig. 1C were obtained from at least 3 different passages of hiPSC lines and their subsequent differentiation into OPCs. RNA sequencing data shown in Fig. 1D–H were generated from 3 independent experiments with 3 different passage numbers of cell lines. Immunostaining images shown in Fig. 2G are representative of a minimum of 3 independent experiments. Representative bright-field and GTTR red fluorescence images in Fig. 4C, D, G, H were collected from at least 3 independent experiments, each with 3 technical replicates. The cell viability and cytotoxicity assay in Fig. 4E, F, I, J, were based on the combined results of at least 3 independent experiments, each with 3–4 technical replicates. The caspase 3/7 results shown in Fig. 5B, C were

based on the combined results of at least 5 independent experiments, each with 3 technical replicates. The immunostaining images shown in Fig. 5E are representative of a minimum of three independent experiments. For the quantification of active mitochondria presented in Fig. 5F, at least 3 images from each of 3 independent experiments were analyzed.

3. Results

3.1. Transcriptomic profiling reveals otic lineage commitment in hiPSC-derived OPCs

We generated OPCs (day 20) from two healthy hiPSC lines (SK8-A and UCSD) through intermediate placode stages (day 14) (Fig. 1A). The differentiation protocol employed a combination of fibroblast growth factors (FGF3 and FGF10) and the Notch inhibitor dibenzazepine (DBZ) (Fig. 1B, C).

To assess the biological relevance of the OPCs and determine whether they mimic key aspects of human inner ear biology, we conducted bulk RNA sequencing on both hiPSCs and their corresponding OPCs derived from two cell lines. PCA revealed distinct global transcriptional profiles between the hiPSC and OPC samples, with mean distance in the PCA space of 176.33 ± 7.38. PERMANOVA analysis confirmed a significant effect of cell type on the overall transcriptomic variance ($F = 23.07$, $R^2 = 0.698$, $P = 0.005$), indicating that approximately 70 % of the observed variance was attributable to differences between hiPSCs and OPCs (Fig. 1D). In contrast, no significant differences were found between the two donor genotypes (UCSD vs. SK8-A; PERMANOVA, $F = 0.81$, $R^2 = 0.075$, $P = 0.615$). This suggests that the transcriptional differences are primarily driven by cell type rather than donor genotype. A total of 7796 differentially expressed genes were identified, including 3483 up- and 4313 down-regulated genes in OPCs compared to hiPSCs ($|\log_2$ fold change >1 and p-adj < 0.005) (Supplementary Table 1). Up-regulated genes included key otic lineage markers such as *PAX2*, *DLX5*, *TBX2*, and *SOX9*, while pluripotency markers such as *NANOG* and *POU5F1* were among the down-regulated genes (Fig. 1E), as noted in prior studies [38–40]. Additionally, a 5.2-fold reduction in *FOXI2* expression suggests that the differentiation process excludes cells of epidermis or epibranchial placode origin, which are developmentally adjacent to otic lineage [41].

To further explore the biological processes related to these transcriptomic changes, we conducted a GO enrichment analysis (Fig. 1F). One of the most enriched GO terms was “Sensory organ development”, alongside terms encompassing the development and morphogenesis of specific tissues, including the ear, inner ear, or auditory receptors (Fig. 1G). Additionally, we identified GO terms related to signaling pathways such as “WNT”, “BMP”, “TGF-β”, and “MAPK”, which are essential for otic placode induction and otocyst formation [42–44]. The identification of the term “Response to retinoic acid (RA)” implies activation of RA signaling, which is known to coordinate the regionalization of the developing ear structures [45,46]. Ingenuity Pathway Analysis (IPA) further revealed up-regulated canonical pathways associated with FGF signaling (essential for initial otic placode specification), Notch signaling (critical for sensory and non-sensory inner ear cell fate determination), and SHH signaling (involved in dorsal and ventral regionalization) [47] (Fig. 1H). Furthermore, 62 genes related to inner ear development (GO:0048839), 7 genes involved in otic vesicle development (GO:0071599), and 5 genes associated

with vestibulocochlear nerve development (GO:0021565) were significantly up-regulated in OPCs compared to hiPSCs (Supplementary Fig. 1A).

To assess the broader suitability of OPCs as a model for human inner ear research, we examined the expression of genes that, when mutated, are associated with SNHL [48]. Interestingly, genes that have been associated with syndromic and non-syndromic SNHL were differentially expressed in OPCs compared to hiPSCs (Supplementary Fig. 1B, C). For example, collagen type II alpha 1 chain (*COL2A1*) and collagen type XI alpha 1 (*COL11A1*), among the highest-expressed syndromic SNHL genes in OPCs, are associated with Stickler syndrome, a connective tissue disorder that includes hearing impairment when the genes are mutated [49]. Among the non-syndromic SNHL genes, gamma-actin gene (*ACTG1*) ranked prominently, with mutations in this gene linked to dominant progressive deafness (DFNA20/26) [50]. These findings support the relevance of OPCs as a model of the human inner ear, as they exhibit the same key cellular and molecular features and may respond similarly to ototoxic agents such as gentamicin.

3.2. Single-cell transcriptomic and protein analysis reveal otic lineage differentiation via placode

To examine how closely OPCs align with the otic lineage beyond SNHL-related gene expression, we tracked their differentiation process through transcriptomic and protein-level analyses. First, we performed scRNA-seq at differentiation days 14 and 20 using two hiPSC lines to comprehensively characterize emerging cell types and their dynamic gene expression profiles. These data were then compared to key in vivo stages of early inner ear development, including non-neural ectoderm, placodal ectoderm, posterior placode, otic-epibranchial placode, otic placode, and otocyst (Fig. 2A).

Following initial quality control and doublet removal (Supplementary Fig. 2A–D), downstream scRNA-seq analyses identified cellular populations based on differentially expressed genes and cell type-specific markers. On day 14 of SK8-A differentiation, UMAP visualization of 5343 cells revealed two major groups: neural ectoderm-originating cells (24.72 %, $PAX6^{+}$, $CDH2^{+}$) [51] and non-neural ectoderm-originating cells (72.96 %, $TFAP2A^{+}$, $CDH1^{+}$) [52] (Fig. 2B, C, and Supplementary Table 2). Additionally, a small, separate cluster (2.32 %) still retained hiPSC stage characteristics ($POU5F1^{+}$), suggesting that the differentiation process was not fully synchronized across all cells.

Within the neural ectoderm group, most cells expressed *PAX6* (85.08 %), a neural plate and neural tube marker [51], and 64.19 % expressed *BMP4* (Supplementary Fig. 2E), which is typically found in the dorsal region of the neural tube, specifically within the roof plate in vivo [53]. Also in this group, a smaller subset of cells expressed markers associated with the neural plate border, which gives rise to neural crest and placodal lineages, including *MSX1* (17.03 %), *ZIC1* (3.18 %), and *PAX3* (1.06 %) [54] (Supplementary Fig. 2E). Although a distinct neural crest cluster was absent, a minor fraction of neural ectoderm-originating cells expressed neural crest markers such as *PLP1* (3.86 %) and *MPZ* (0.30 %) [55] (Supplementary Fig. 2E). These findings suggest that under our differentiation conditions, most neural plate border-like cells may preferentially adopt a placodal-like fate rather than differentiating into neural crest cells.

The non-neural ectoderm group further diversified into placodal-like cells (29.29 %) and otic epithelial-like cells (43.66 %, *EPCAM*$^+$, *FBXO2*$^+$) (Fig. 2C). The placode groups included *IRX3*$^+$ posterior placode-like cells (41.02 %) [56], *SPRY1*$^+$ otic-epibranchial-like cells (42.62 %), and *COL2A1*$^+$ otic placode-like cells (85.24 %) (Fig. 2C). However, anterior placode markers were less expressed, including *OTX2* (23.26 %), *SIX3* (25.30 %), and *PAX6* (9.58 %) [56] (Supplementary Table 2). A similar cell type composition was observed in the UCSD line on day 14, consisting of neural ectoderm- (11.42 %), placode- (23.32 %), and otic epithelial-like cells (56.14 %) (Supplementary Fig. 2F). Compared to the SK8-A line, the UCSD line had a lower proportion of neural ectoderm-origin cells (11.42 % vs. 24.72 %) and higher otic lineage representation (56.14 % vs. 43.66 %).

On day 20 in the SK8-A line, 82.96 % of total 5621 cells were classified as otic lineage, identified by *EPCAM* and *FBXO2* expression (Fig. 2D, E), well known otic epithelium markers present in floor epithelium (interdental cells, organ of Corti, etc.) and roof epithelium (stria vascularis, Reissner's membrane, etc.) at 15–23 weeks of human gestation [57]. Within the otic clusters, additional genes such as *LUM* (76.43 %), *APOE* (91.79 %), *FSTL1* (68.48 %), and *IGFBP3* (57.77 %) were expressed, consistent with human fetal otic epithelium [57] (Supplementary Fig. 2G). These were co-expressed with otic lineage-specific genes systemically identified in mice by Hartman et al. [58], such as *CLDN6* (77.35 %), *WFDC2* (56.27 %), *CD9* (57.75 %), and *RAB25* (55.84 %) (Supplementary Fig. 2G). While distinct inner ear regions were not mapped as a separate cluster, such as hair cells (Supplementary Fig. 2H), expression of floor epithelium-related genes was greater than that of roof epithelium markers (Fig. 2F). The remaining non-otic cells included neural ectoderm- (5.48 %, *PAX6*$^+$), mesenchyme- (6.37 %, *LRRC75A*$^+$, *CTNNB1*$^+$) [59,60], and epithelial mesenchymal transition (EMT)-like cells (5.19 %, *GDF15*$^+$, *TWIST1*$^+$) [61,62], which contribute to otic placode induction and inner ear morphogenesis [63]. In the UCSD line on day 20, differentiation efficiency was even higher, with 94.57 % of cells classified as otic-related, while only small fractions represented mesenchyme- (3.59 %), EMT- (1.58 %), and neural ectoderm-like cells (0.25 %) (Supplementary Fig. 2I).

To correlate gene expression patterns with protein expression, we conducted immunostaining. At the placode stage (day 14), cells expressed non-neural ectoderm and neural plate border origin markers (SK8-A: 58.35 ± 10.2 % TFAP2A$^+$, 54.47 ± 12.72 % GATA3$^+$; UCSD: 55.26 ± 1.92 % TFAP2A$^+$, 55.78 ± 8.85 % GATA3$^+$), as well as otic-epibranchial placode markers (SK8-A: 19.29 ± 4.70 % SPRY1$^+$; UCSD: 12.98 ± 6.82 % SPRY1$^+$) (Supplementary Fig. 3). By day 20, otic epithelium markers were highly expressed (SK8-A: 96.33 ± 0.58 % EPCAM, 94.75 ± 4.11 % FBXO2; UCSD: 94.85 ± 1.51 % EPCAM$^+$, 98.50 ± 0.59 % FBXO2$^+$) [58,64], along with floor epithelium (SK8-A: 93.17 ± 3.02 % GATA3$^+$; UCSD: 84.31 ± 4.34 % GATA3$^+$) and pro/sensory markers (SK8-A: 23.79 ± 3.43 % PROX1$^+$; UCSD: 25.11 ± 4.28 % PROX1$^+$) [65,66] (Fig. 2G). Together, these transcriptomic and protein expression data indicate that over 83 % of cells from both hiPSC lines differentiated toward the otic lineage through placode, recapitulating critical stages of early human inner ear development.

3.3. Cell-cell communication analysis highlights interactions between otic lineage and neighboring cells

To better understand interactions between various cell types during OPC differentiation, we analyzed the expression of distinct signaling molecules and receptors using CellChat [33]. We first integrated scRNA-seq data from SK8-A day 14 and day 20 and classified cells into five major groups: Otic, Placode, Neural ectoderm, Mesenchyme, and EMT (Fig. 3A). CellChat analysis revealed that the Mesenchyme and Placode groups were heavily engaged in cell communication. Mesenchyme secreted signals through 506 ligand-receptor pairs and Placode secreted signals through 357 ligand-receptor pairs, while they received signals through 446 and 372 ligand-receptor pairs, respectively (Fig. 3B). The strongest interaction was observed from the Mesenchyme to the Placode group (Fig. 3B).

Overall, 33 signaling pathways were identified in the intercellular communication network (Fig. 3C). These pathways included key signaling networks critical for placode induction to inner ear development. Specifically, outgoing communication patterns showed that mesenchyme cells were the primary source of all secreted signals, and neural ectoderm cells also contributed to release signals promoting otic placode/vesicle development, including FGF, WNT, and BMP pathways. Correspondingly, incoming communication patterns indicated that the otic placode was regulated by those three signaling pathways.

FGFs are well-established inducers of the otic placode during inner ear development. In mice, FGF3, FGF10, and FGF8 play crucial roles in the early induction of the otic placode [67–69]. Consistent with this, our data identified FGF signaling as one of the most abundant signaling interactions across all five groups (Fig. 3C). Ligand-receptor interaction analysis revealed that multiple FGF ligands (*FGF1–10*), secreted by the Neural ectoderm, Mesenchyme, and EMT, contributed to otic placode induction (Fig. 3D, E). This finding aligns with the established role of FGFs, secreted by the hindbrain and mesenchyme, in initiating placode specification [70,71]. In addition, in the Otic group, *FGFR2*, *FGFR3*, and *FGFR4* were identified as receptors for FGFs secreted primarily by the Neural Ectoderm. Considering that cells in the mouse otic vesicles expressing *Fgfr1*, *Fgfr2*, and *Fgfr3* are located medio-anterior, dorso-medial, and latero-anterior, respectively [72], these results suggest that human OPCs may also contain regionally specified cell populations.

WNT signaling is another critical pathway for otic commitment. CellChat analysis identified *WNT3A* (from the Neural ectoderm) and *WNT3A/WNT6* (from the Mesenchyme) as the primary ligands interacting with FZD and LRP receptors in the Placode (Fig. 3E). This aligns with previous findings in chicken and mouse models showing that WNT signaling promotes otic placode formation from the posterior placode, whereas its inhibition favors the development of epibranchial placodes within the otic-epibranchial placode domain [42,73]. Conversely, WNT signals from the Otic and Placode groups interacted with their corresponding receptors in the Mesenchyme, consistent with the known role of canonical Wnt signaling from the cochlear duct epithelium in the development of the periotic mesenchyme in mice [60].

We also identified BMP signaling activity, with *BMP2*, *BMP4*, *BMP7*, *GDF5*, and *GDF6* secreted by the Neural ectoderm and/or Mesenchyme (Fig. 3E). These ligands interacted

with their receptors, such as *BMPR* and *ACVR*, in the Placode and Otic groups. The Neural ectoderm to Placode BMP signaling is consistent with findings that *BMP4* expression in the dorsal neural tube patterns the ectoderm during gastrulation to induce the development of placode in Xenopus and chicken [74,75]. Additionally, BMP interactions between the Neuroectoderm/Mesenchyme and Otic are consistent with studies in chicken showing that *Bmp4* and *7*, expressed in mesenchyme adjacent to the otocyst, play a major role in dorsal otocyst patterning [76]. Moreover, mutations in *GDF6* lead to cochlear aplasia in both mouse models and humans [77]. Although BMP regulators such as Noggin in the otic mesenchyme or otocyst have been observed to tightly regulate BMP signaling in chicken [78,79], our analysis did not identify these inhibitory pathways.

Lastly, TGF-β signaling, particularly *Tgfb2,* is known to promote senescence in the developing inner ear, which is crucial for the closure of the otic pore and shaping the otic vesicle [80]. In our CellChat analysis, *TGFB1*, *TGFB2*, and *TGFB3*, primarily secreted by the mesenchyme, were found to interact with their receptors in the Placode and Otic groups (Fig. 3E). Together, these findings suggest that a balance between FGF, WNT, BMP, and TGF-β signaling is essential for OPC differentiation, similar to what is observed during inner ear development in vivo.

3.4. Gentamicin C2b maintains antibacterial efficiency and induces lower toxicity in human OPCs

Having characterized the OPC model and component cell populations, we next investigated whether gentamicin C2b exhibits reduced ototoxicity compared to clinical gentamicin in human OPCs (Fig. 4A). First, we assessed the antimicrobial activity of both clinical gentamicin and gentamicin C2b in vitro. Using 4 different *E. coli* strains (Stbl3, Top10, Mach1, and Omni), we tested a range of gentamicin and gentamicin C2b concentrations (0–40 μg/mL). No significant differences in antibacterial efficiency were observed between gentamicin and gentamicin C2b (Fig. 4B), consistent with previous reports [25].

We then selected a concentration range of 0–500 μg/mL gentamicin to encompass the previously reported half-maximal inhibitory concentration (IC_{50}) for mouse outer hair cell survival (563 ± 28 μM [estimated at 268.9 μg/mL]) [25] and human OPC viability (472.17 ± 75.21 μM [218.0 ± 34.8 μg/mL]) [31] post-gentamicin exposure. The cells were exposed to gentamicin or gentamicin C2b for 24 h, a duration previously shown to elicit clear dose-dependent effects in OPCs [31].

Previous studies have reported that gentamicin does not induce toxicity in human embryonic stem cells [81] or hiPSCs [31]. Therefore, as a control, we examined the effects of gentamicin on hiPSCs, observing that no visible damage was observed on phase-contrast images even at the highest gentamicin concentration (500 μg/mL) (Fig. 4C). To assess whether the lack of toxicity was due to failure of gentamicin uptake, we treated hiPSCs with GTTR, a fluorescently labeled conjugate of gentamicin with Texas Red. No red fluorescence was detected in hiPSCs after 24 h of GTTR exposure (Fig. 4D), confirming no gentamicin internalization. These findings were corroborated by cell viability and cytotoxicity assays, which showed no significant differences between vehicle-treated controls and gentamicin-exposed groups (Fig. 4E, F). Specifically, when normalized to control (set as 100 %), cell

viability did not decrease even at 500 μg/mL gentamicin (SK8-A hiPSC: 101.10 ± 22.62 %; UCSD hiPSC: 101.94 ± 12.93 %) (Fig. 4E). Similarly, cytotoxicity remained at baseline levels for SK8-A (0.92 ± 0.07) and UCSD (1.06 ± 0.07) hiPSCs (control set as 1) at 500 μg/mL gentamicin (Fig. 4F).

In contrast, OPCs exhibited clear uptake of GTTR after 24 h of exposure, as indicated by cytoplasmic fluorescence (Fig. 4G), suggesting an active gentamicin internalization mechanism. Supporting this observation, compared to hiPSCs, OPCs exhibited greater up-regulation of multiple gentamicin uptake-related genes. Specifically, TRP channels such as *TRPC4* and *TRPM4*, ATP receptor genes such as *P2RY2* and *P2RY6*, and numerous genes involved in endocytic uptake (e.g., *LRP1*, *LRP2*, *EGFR*, *CD36*, *CUBN*, *SORT1*, and *NPR3*) were elevated in OPCs (Supplementary Fig. 4A). Moreover, genes associated with the GO term “response to antibiotic,” including *JAK1*, *JAK2*, *GRIA1*, *KDM6B*, and *SLC9A1,* were up-regulated in OPCs compared to hiPSCs (Supplementary Fig. 4B). This transcriptional profile suggests that OPCs may have an intrinsically greater capacity to internalize and respond to gentamicin exposure.

Morphological assessment revealed that OPCs exposed to 500 μg/mL gentamicin for 24 h appeared rounded and swollen, indicative of extensive cell death [82] (Fig. 4H). Cell viability decreased in a dose-dependent manner, beginning at 50 μg/mL gentamicin, in both OPC lines compared to controls. Statistical analysis confirmed significant reductions in cell viability beginning at 50 μg/mL for SK8-A ($P < 0.01$) and at 500 μg/mL for UCSD ($P < 0.01$) (Fig. 4I and Supplementary Fig. 4C). Indeed, SK8-A OPCs exhibited significantly higher expression levels of several endocytic receptor genes, including *LRP1*, *TFRC*, *EGFR*, and *NPR3* ($\log_2$ fold change > 1 and p-adj < 0.05), compared to UCSD OPCs (Supplementary Fig. 4D). This elevated expression of endocytic receptors in the SK8-A line may facilitate the cellular entry of the aminoglycoside, contributing to the observed increased cytotoxicity. Consistent with the cell viability findings, cytotoxicity measured by LDH release, which is an indicator of necrosis or late-stage apoptosis [83], increased in a dose-dependent manner following gentamicin exposure (Fig. 4J). Specifically, in SK8-A OPCs, cytotoxicity significantly increased versus control beginning at 50 μg/mL ($P < 0.05$), reaching 2.25-fold higher than control at 500 μg/mL gentamicin (Supplementary Fig. 4E). In UCSD OPCs, cytotoxicity significantly increased versus control beginning at 100 μg/mL gentamicin ($P < 0.05$), reaching 1.85-fold higher cytotoxicity than control at 500 μg/mL gentamicin.

However, gentamicin C2b induced lower cytotoxicity than gentamicin across all tested concentrations. Cell viability remained higher in gentamicin C2b-exposed groups in both OPC lines (Fig. 4I). Even at 500 μg/mL, cell viability in the gentamicin C2b-treated OPCs was dramatically higher (SK8-A: 94.52 %; UCSD: 84.93 %) compared to the gentamicin-treated OPCs (SK8-A: 19.06 %, $P < 0.001$; UCSD: 30.38 %, $P < 0.01$). Similarly, cytotoxicity was markedly lower in the gentamicin C2b-exposed groups, with reductions observed in SK8-A from 50 μg/mL onward ($P < 0.05$) and in UCSD from 250 μg/mL onward ($P < 0.05$) (Fig. 4J). At 500 μg/mL, cytotoxicity in gentamicin C2b-treated OPCs was only 1.19-fold (SK8-A) and 1.15-fold (UCSD) higher than control, a stark contrast to the effects observed with clinical gentamicin. Together, these findings

indicate that gentamicin C2b induces less toxicity in human OPCs compared to clinical gentamicin, resulting in better preservation of metabolic activity and membrane integrity across concentrations ranging from 50 to 500 μg/mL.

3.5. Gentamicin C2b induces less mitochondrial-dependent apoptosis in OPCs

Apoptosis is the predominant form of sensory cell death in the inner ear following gentamicin exposure [84]. Therefore, we measured caspase 3/7 activity, a key indicator of apoptotic cell death to assess whether gentamicin C2b induces less apoptosis than clinical gentamicin in OPCs (Fig. 5A).

Using real-time live cell imaging, we monitored the rate and extent of caspase 3/7 activity in SK8-A OPCs over 24 h of exposure to gentamicin or gentamicin C2b at 250 and 500 μg/mL. In the gentamicin-treated groups, caspase 3/7 activity progressively increased over time, with significant elevations observed between 11 and 24 h at 250 μg/mL ($P < 0.05$) and between 9 and 24 h at 500 μg/mL ($P < 0.05$) compared to the control (Fig. 5B). In contrast, caspase 3/7 activity remained relatively stable in the gentamicin C2b-treated groups and showed no significant difference from the control.

When comparing gentamicin and gentamicin C2b exposure, significant differences in caspase 3/7 activity emerged at 14 h onward for 250 μg/mL ($P < 0.05$) and 10 h onward for 500 μg/mL ($P < 0.05$). At 24 h post-exposure, the gentamicin C2b-exposed groups had notably less activated caspase 3/7 compared to the gentamicin-treated groups (as indicated by green fluorescent signal in Fig. 5C). The average caspase 3/7 counts were significantly higher in gentamicin-treated OPCs (716.17 at 250 μg/mL; 756.17 at 500 μg/mL) compared to both gentamicin C2b-treated OPCs (336 at 250 μg/mL; 367.67 at 500 μg/mL) and control (346.5) (Fig. 5D).

Caspase 3/7 activation by gentamicin in the inner ear is closely linked to mitochondrial-dependent apoptosis [84]. Gentamicin induces ototoxicity primarily through oxidative stress, which leads to mitochondrial dysfunction, the release of cytochrome c [85], and the activation of mitochondrial apoptotic pathways [31,84]. To evaluate whether gentamicin C2b induces less disruption of mitochondrial transmembrane potential compared to gentamicin, we used the Mito-Tracker fluorescent probe. Mito-Tracker staining showed that filamentous-appearing mitochondria were distributed relatively homogeneously around the cell nucleus in the control and gentamicin C2b-exposed groups after 24 h in both OPC lines (Fig. 5E). However, this homogenous mitochondrial distribution was disrupted in gentamicin-exposed OPCs.

To quantify mitochondrial integrity per cell, we measured the Mito-Tracker positive area and divided it by the number of DAPI-stained nuclei. Following 24 h of exposure to 500 μg/mL gentamicin, mitochondrial signal levels were reduced to 35.98 ± 2.53 % in SK8-A ($P < 0.0001$) and 34.66 ± 7.53 % in UCSD ($P < 0.0001$) compared to vehicle-treated control (Fig. 5F). However, at 500 μg/mL gentamicin C2b, the reduction was less pronounced and did not significantly differ from control, with mitochondrial signal of 93.13 ± 5.99 % in SK8-A ($P = 0.14$) and 92.96 ± 1.46 % in UCSD ($P = 0.21$). Furthermore, at 24 h post-exposure, we observed cytochrome c expression throughout the cytoplasm in gentamicin-exposed OPCs,

indicating its release from mitochondria. In contrast, in gentamicin C2b-exposed and control OPCs, cytochrome c expression mostly remained co-localized with Mito-Tracker, suggesting its retention within mitochondria.

Together, the better-preserved Mito-Tracker signal, indicative of an intact mitochondrial membrane potential, along with the retention of cytochrome c within mitochondria, demonstrates that gentamicin C2b induces less mitochondrial dysfunction and resultant apoptosis compared to clinical gentamicin in human OPCs.

3.6. Comparative impact of clinical gentamicin and gentamicin C2b on hearing function in mice in vivo

In addition to establishing the cellular-level ototoxicity of the two gentamicin preparations, we also evaluated their impact on the hearing function of mice *in vivo* (Fig. 6A). Because systemic administration of gentamicin does not result in hearing deficits in mice, we applied gelatin sponges soaked with 200 mg/mL gentamicin, 200 mg/mL gentamicin C2b, or saline (control) directly to the round window niche of the cochlea, a technique previously reported to induce cochlear hair cell damage in mice [36].

Hearing function was assessed preoperatively (baseline) and at 1 and 2 weeks post-gelatin sponge application using ABR and DPOAE measurements (Fig. 6B, C and Supplementary Fig. 5A, B). At both post-baseline assessment points, mice exposed to gentamicin exhibited significant and progressive threshold elevations across all tested frequencies in ABR recordings. In contrast, although the gentamicin C2b-exposed group also displayed a significant threshold elevation, primarily at high frequencies, this increase was markedly milder compared to the robust elevation observed in the gentamicin group. Saline-treated controls showed no significant changes (Supplementary Fig. 5A). These findings were consistent with the DPOAE results, where the gentamicin-exposed group had progressive threshold elevation across all frequencies while both the saline and gentamicin C2b groups showed no significant threshold changes from baseline (Supplementary Fig. 5B).

To correlate these functional findings with histological changes, we performed immunostaining on cochlear whole mounts from the exposed mice, using MYO7A as a hair cell marker. Both the saline and gentamicin C2b groups showed almost no outer hair cell loss across cochlear regions. The percentages of outer hair cell survival in saline and C2b are 100.0 ± 0.00 % vs 100.0 ± 0.00 % at 11.33 kHz, 100.0 ± 0.00 % vs 100.0 ± 0.00 % at 22.65 kHz, and 99.54 ± 0.463 % vs 97.69 ± 1.39 % at 45.25 kHz, respectively. In contrast, the gentamicin-treated group demonstrated a characteristic base-to-apex gradient of outer hair cell loss: 99.58 ± 0.417 % at 11.33 kHz, 93.60 ± 1.96 % at 22.65 kHz, and 29.33 ± 9.45 % at 45.25 kHz (Fig. 6D).

Quantitative analysis confirmed significantly greater outer hair cell survival in the gentamicin C2b group compared to the gentamicin at 22.65 kHz (located near the boundary between the middle and basal turns; $P = 0.0078$), and 45.25 kHz (within the basal turn, closer to the hook portion; $P < 0.0001$) (Fig. 6D, E). These results indicate that gentamicin C2b induces less functional and structural damage to cochlear hair cells compared to

conventional gentamicin, consistent with our observations regarding its lower ototoxicity in human OPCs.

4. Discussion

In this study, we demonstrate the reduced ototoxic effects of gentamicin C2b compared to clinical gentamicin by assessing cellular toxicity in a human inner ear model in vitro and hearing function in a mammalian model in vivo. Our findings suggest that gentamicin C2b may be a safer alternative to conventionally used gentamicin and may better preserve auditory function without compromising antimicrobial efficacy.

To establish a relevant human inner ear model for assessing the ototoxicity of gentamicin and its C2b component, we generated OPCs from hiPSCs and performed a comprehensive characterization. By day 14 of differentiation, approximately 73 % (SK8-A) and 79 % (UCSD) of the cells originated from non-neural ectoderm and differentiated through the placodal stage toward otic lineage-like cell types, rather than differentiating into neural crest or other placode-derived sensory/non-sensory lineages. By day 20, 83 % (SK8-A) and 95 % (UCSD) of the cells expressed genes associated with otic development, consistent with profiles observed in fetal otic epithelium [57]. Using GTTR, we demonstrated that these human OPCs are capable of internalizing gentamicin. Additionally, transcriptomic profiling revealed up-regulation of several genes associated with gentamicin uptake pathways in OPCs. While gentamicin entry into inner ear cells may occur through various mechanisms [86], including specific channels, receptors, or endocytosis, our data suggested that receptor-mediated endocytosis could be the predominant pathway in OPCs. Specifically, we observed significant up-regulation of *LRP2* (encoding megalin), a well-established endocytic receptor implicated in gentamicin uptake in the cochlea [87]. The inhibition of megalin has previously been shown to confer otoprotection [87]. The concurrent up-regulation of *CUBN* (encoding cubilin) in OPCs further supports this mechanism, as megalin and cubilin frequently function in endocytosis and have both been localized in multiple cell types of the human cochlea and vestibular organs [88].

To our best knowledge, this study provides the first evidence that gentamicin C2b exhibits significantly reduced ototoxicity in human inner ear models. OPCs treated with gentamicin C2b displayed higher cell viability, lower cytotoxicity, less mitochondrial dysfunction, and reduced apoptosis compared to those treated with clinically used gentamicin. While OPCs are immature, our data demonstrate that they are nonetheless a valuable platform not only for the study of early otic lineage differentiation, but also for evaluating ototoxicity relevant to clinical drug screening. This finding is in line with the accumulating evidence indicating that immature hiPSC-derived cell models can robustly recapitulate key aspects of disease-related cellular stress and drug responses. For example, previous studies have demonstrated that three-dimensional neural tissues derived from hiPSCs, including cortical neurons, faithfully model pathological processes observed in late-stage neurodegenerative diseases such as Alzheimer’s disease, and have been successfully used for translational drug screening [89–92]. Furthermore, in the auditory field, immature cochlear explant models in mice have similarly proven useful for drug screening, with compounds identified in these

early-stage systems subsequently demonstrating efficacy in mature in vivo animal models [37].

Importantly, this study provides complementary evidence in mice that exposure to gentamicin C2b demonstrated better preservation of outer hair cells both morphologically and functionally, with only mild auditory threshold shifts at high frequencies that did not significantly differ from saline-treated controls. However, the slight elevation of ABRs at high frequency regions of the cochlea suggests minor damage, potentially involving cochlear hair cells or synaptic connections between hair cells and auditory neurons. In contrast, mice treated with gentamicin exhibited substantially elevated thresholds in both ABR and DPOAE recordings across all tested frequencies. Particularly, the marked increase in DPOAE thresholds indicates widespread cochlear dysfunction, primarily affecting outer hair cells.

Interestingly, histological analysis revealed a gradient of outer hair cell loss, progressing from the basal to the apical turn of the cochlea. This could be due to gentamicin application to the round window at the base of the cochlea, which is adjacent to the region encoding high frequencies. In addition, basal outer hair cells are considered more metabolically vulnerable to environmental changes [93], more susceptible to free radicals [94], and to failure of calcium homeostasis [95]. Yet MYO7A immunostaining labels hair cell bodies but may not detect subtle subcellular damage, while DPOAE measurement reflects not only the presence but also the functional integrity of outer hair cells. Even morphologically intact outer hair cells may exhibit impaired electro-motility function due to sublethal damage such as mitochondrial dysfunction, loss of stereocilia integrity or tip links, or synaptic abnormalities, any of which could result in elevated DPOAE thresholds.

Ototopical administration of gentamicin, such as ear drops, rather than intravenous or intramuscular administration, is the closest clinical setting comparable to our in vitro and in vivo exposures. In clinical practice, topical gentamicin is frequently prescribed for conditions such as chronic otitis externa, otitis media with tympanostomy tubes, and post-operative prophylaxis [96]. The typical concentration of ototopical gentamicin is 0.3 % gentamicin sulfate, equivalent to approximately 3 mg/mL [97]. Although a direct comparison between clinical concentrations and those used in experimental models is inherently limited by differences in drug distribution and exposure duration, our findings revealed that gentamicin induced ototoxic effects in human OPCs at 50 μg/mL, a concentration lower than that used in clinical ototopical formulations. While topical gentamicin is generally regarded as safe when the tympanic membrane is intact, the risk of ototoxicity increases in cases of tympanic membrane perforation [98]. A literature review identified 54 cases of gentamicin-associated vestibular toxicity following ototopical administration, with 24 of these cases also presenting cochlear toxicity, indicating a combined vestibulo-cochlear toxicity rate of over 44 % among affected individuals [97]. Notably, in our in vivo model, application of 1 μl of 200 mg/mL of gentamicin C2b (equivalent to 200 μg total) to the round window in mice resulted in only minor auditory threshold shifts both in ABR and DPOAE measurements. These findings highlight the clinical relevance of our experimental model and support the development of safer

aminoglycoside formulations that reduce inner ear toxicity while preserving antimicrobial efficacy.

5. Conclusions

Taken together, our results indicate that gentamicin C2b is associated with reduced ototoxicity and greater preservation of hearing function as compared to clinically used gentamicin in human cellular and animal models, while retaining its antimicrobial efficacy. This study underscores the value of combining hiPSC-derived human inner ear models with in vivo analyses to assess the ototoxicity of existing medications as well as the translational potential of otoprotective compounds. The human OPC model offers several practical advantages: quick differentiation time (20 days), ease of use, scalability, potential for high-throughput drug screening and fast iteration because of robust readouts, rapid mechanistic insights, human relevance, and ethical alignment to replace, reduce and refine animal research. Further, our findings provide strong foundational evidence to support clinical trials of gentamicin C2b as a potentially safer alternative for patients requiring aminoglycoside treatment, particularly those at higher risk for hearing loss, such as pediatric and geriatric populations or individuals with preexisting cochlear damage.

Supplementary Material

Refer to Web version on PubMed Central for supplementary material.

Acknowledgments

We would like to thank Dr. Marie Kubota and the MGH sequencing core facility for their assistance in analyzing scRNA-seq data, and Dr. Anthony Ricci for providing some gentamicin C2b. We are also grateful to Dr. Svetolik Spasic for conducting a pilot in vivo study. Additionally, we thank Dr. Shelley Batts for critical review and editing of the manuscript.

Funding

This work was supported by the National Institutes of Health grants U24 DC020857 and R01 DC021133, the Remondi Foundation, and Bertarelli Foundation endowed professorship (all awarded to K.M.S.). M. S. was supported in part by the Uehara Memorial Foundation.

Data availability

Data will be made available on request.

References

[1]. Weinstein MJ, Luedemann GM, Oden EM, Wagman GH, Rosselet JP, Marquez JA, et al. , Gentamicin, a new antibiotic complex from micromonospora, J. Med. Chem 6 (1963) 463–464. [PubMed: 14184912]

[2]. Kushner B, Allen PD, Crane BT, Frequency and demographics of gentamicin use, Otol. Neurotol 37 (2) (2016) 190–195. [PubMed: 26719956]

[3]. Phillips I, Eykyn S, King BA, Jenkins C, Warren CA, Shannon KP, The in vitro antibacterial activity of nine aminoglycosides and spectinomycin on clinical isolates of common Gram-negative bacteria, J. Antimicrob. Chemother 3 (5) (1977) 403–410. [PubMed: 143468]

[4]. Prins JM, Buller HR, Kuijper EJ, Tange RA, Speelman P, Once versus thrice daily gentamicin in patients with serious infections, Lancet 341 (8841) (1993) 335–339. [PubMed: 8094114]

[5]. Organization WH. Essential Medicines List includes Gentamicin injection for use during pregnancy, childbirth and postpartum care. [Available from: 〈https://www.who.int/data/gho/indicator-metadata-registry/imr-details/essential-medicines-list-includes-gentamicin-injection-for-use-during-pregnancy-childbirth-and-postpartum-care〉 .

[6]. Wersall J, Lundquist PG, Bjorkroth B, Ototoxicity of gentamicin, J. Infect. Dis 119 (4) (1969) 410–416. [PubMed: 5305936]

[7]. Jackson GG, Arcieri G, Ototoxicity of gentamicin in man: a survey and controlled analysis of clinical experience in the United States, J. Infect. Dis 124 (1971) S130–S137. [PubMed: 5126239]

[8]. Moffat DA, Ramsden RT, Profound bilateral sensorineural hearing loss during gentamicin therapy, J. Laryngol. Otol 91 (6) (1977) 511–516. [PubMed: 874379]

[9]. Rizzi MD, Hirose K, Aminoglycoside ototoxicity, Curr. Opin. Otolaryngol. Head. Neck Surg 15 (5) (2007) 352–357. [PubMed: 17823553]

[10]. Govaerts PJ, Claes J, van de Heyning PH, Jorens PG, Marquet J, De Broe ME, Aminoglycoside-induced ototoxicity, Toxicol. Lett 52 (3) (1990) 227–251. [PubMed: 2202080]

[11]. Chaves BJ, Tadi P, Gentamicin, StatPearls, Treasure Island (FL), 2024.

[12]. Cabanas MJ, Vazquez D, Modolell J, Inhibition of ribosomal translocation by aminoglycoside antibiotics, Biochem Biophys. Res. Commun 83 (3) (1978) 991–997. [PubMed: 361042]

[13]. Alharazneh A, Luk L, Huth M, Monfared A, Steyger PS, Cheng AG, et al. , Functional hair cell mechanotransducer channels are required for aminoglycoside ototoxicity, PLoS One 6 (7) (2011) e22347. [PubMed: 21818312]

[14]. Lee JH, Park C, Kim SJ, Kim HJ, Oh GS, Shen A, et al. , Different uptake of gentamicin through TRPV1 and TRPV4 channels determines cochlear hair cell vulnerability, Exp. Mol. Med 45 (3) (2013) e12. [PubMed: 23470714]

[15]. Lin SCY, Thorne PR, Housley GD, Vlajkovic SM, Purinergic signaling and aminoglycoside ototoxicity: the opposing roles of P1 (Adenosine) and P2 (ATP) receptors on cochlear hair cell survival, Front Cell Neurosci 13 (2019) 207. [PubMed: 31156393]

[16]. Hashino E, Shero M, Endocytosis of aminoglycoside antibiotics in sensory hair cells, Brain Res 704 (1) (1995) 135–140. [PubMed: 8750975]

[17]. Hodiamont CJ, van den Broek AK, de Vroom SL, Prins JM, Mathot RAA, van Hest RM, Clinical pharmacokinetics of gentamicin in various patient populations and consequences for optimal dosing for gram-negative infections: an updated review, Clin. Pharm 61 (8) (2022) 1075–1094.

[18]. Jana S, Crich D, Synthesis of gentamicin minor components: gentamicin C1a and gentamicin C2b, Org. Lett 24 (46) (2022) 8564–8567. [PubMed: 36375034]

[19]. Li S, Guo J, Reva A, Huang F, Xiong B, Liu Y, et al. , Methyltransferases of gentamicin biosynthesis, Proc. Natl. Acad. Sci. USA 115 (6) (2018) 1340–1345. [PubMed: 29358400]

[20]. Forge A, Schacht J, Aminoglycoside antibiotics, Audio Neurootol 5 (1) (2000) 3–22.

[21]. Hobbie SN, Akshay S, Kalapala SK, Bruell CM, Shcherbakov D, Bottger EC, Genetic analysis of interactions with eukaryotic rRNA identify the mitoribosome as target in aminoglycoside ototoxicity, Proc. Natl. Acad. Sci. USA 105 (52) (2008) 20888–20893. [PubMed: 19104050]

[22]. Okachi R, Kawamoto I, Takasawa S, Yamamoto M, Sato S, A new antibiotic XK-62–2 (Sagamicin). I. Isolation, physicochemical and antibacterial properties, J. Antibiot 27 (10) (1974) 793–800.

[23]. Akiyoshi M, Hara T, [Animal test for evaluation of ototoxicity and safety of KW-1062 (author's transl)], Jpn J. Antibiot 33 (2) (1980) 219–226. [PubMed: 7373855]

[24]. Akiyoshi M, Nakada H, Akashi O, Waki Y, Hara T, Harada S, et al. , [Evaluation of ototoxic effect of micronomicin by intravenous drip infusion], Jpn J. Antibiot 38 (2) (1985) 203–211. [PubMed: 3874294]

[25]. O'Sullivan ME, Song Y, Greenhouse R, Lin R, Perez A, Atkinson PJ, et al. , Dissociating antibacterial from ototoxic effects of gentamicin C-subtypes, Proc. Natl. Acad. Sci. USA 117 (51) (2020) 32423–32432. [PubMed: 33288712]

[26]. Chatterjee S, Lufkin T, The sound of silence: mouse models for hearing loss, Genet. Res. Int 2011 (2011) 416450. [PubMed: 22567353]

[27]. Poirrier AL, Van den Ackerveken P, Kim TS, Vandenbosch R, Nguyen L, Lefebvre PP, et al. , Ototoxic drugs: difference in sensitivity between mice and guinea pigs, Toxicol. Lett 193 (1) (2010) 41–49. [PubMed: 20015469]

[28]. Lahlou H, Lopez-Juarez A, Fontbonne A, Nivet E, Zine A, Modeling human early otic sensory cell development with induced pluripotent stem cells, PLoS One 13 (6) (2018) e0198954. [PubMed: 29902227]

[29]. Jeong M, Ocwieja KE, Han D, Wackym PA, Zhang Y, Brown A, et al. , Direct SARS-CoV-2 infection of the human inner ear may underlie COVID-19-associated audiovestibular dysfunction, Commun. Med 1 (1) (2021) 44. [PubMed: 34870285]

[30]. Harding AT, Ocwieja K, Jeong M, Zhang Y, Leger V, Jhala N, et al. , Human otic progenitor cell models of congenital hearing loss reveal potential pathophysiologic mechanisms of Zika virus and cytomegalovirus infections, mBio 15 (4) (2024) e0019924. [PubMed: 38440980]

[31]. Jeong M, Kurihara S, Stankovic KM, An in vitro oxidative stress model of the human inner ear using human-induced pluripotent stem cell-derived otic progenitor cells, Antioxidants 13 (11) (2024).

[32]. McGinnis CS, Murrow LM, Gartner ZJ, DoubletFinder: doublet detection in single-cell RNA sequencing data using artificial nearest neighbors, Cell Syst 8 (4) (2019) 329–337.e4. [PubMed: 30954475]

[33]. Jin S, Guerrero-Juarez CF, Zhang L, Chang I, Ramos R, Kuan CH, et al. , Inference and analysis of cell-cell communication using CellChat, Nat. Commun 12 (1) (2021) 1088. [PubMed: 33597522]

[34]. Seist R, Landegger LD, Robertson NG, Vasilijic S, Morton CC, Stankovic KM, Cochlin deficiency protects against noise-induced hearing loss, Front. Mol. Neurosci 14 (2021) 670013. [PubMed: 34108864]

[35]. Chen J, Landegger LD, Sun Y, Ren J, Maimon N, Wu L, et al. , A cerebellopontine angle mouse model for the investigation of tumor biology, hearing, and neurological function in NF2-related vestibular schwannoma, Nat. Protoc. 14 (2) (2019) 541–555. [PubMed: 30617350]

[36]. Heydt JL, Cunningham LL, Rubel EW, Coltrera MD, Round window gentamicin application: an inner ear hair cell damage protocol for the mouse, Hear Res 192 (1–2) (2004) 65–74. [PubMed: 15157964]

[37]. Seist R, Tong M, Landegger LD, Vasilijic S, Hyakusoku H, Katsumi S, et al. , Regeneration of cochlear synapses by systemic administration of a bisphosphonate, Front. Mol. Neurosci 13 (2020) 87. [PubMed: 32765216]

[38]. Noramly S, Grainger RM, Determination of the embryonic inner ear, J. Neurobiol 53 (2) (2002) 100–128. [PubMed: 12382270]

[39]. Song H, Morrow BE, Tbx2 and Tbx3 regulate cell fate progression of the otic vesicle for inner ear development, Dev. Biol 494 (2023) 71–84. [PubMed: 36521641]

[40]. Mak AC, Szeto IY, Fritzsch B, Cheah KS, Differential and overlapping expression pattern of SOX2 and SOX9 in inner ear development, Gene Expr. Patterns 9 (6) (2009) 444–453. [PubMed: 19427409]

[41]. Jayasena CS, Ohyama T, Segil N, Groves AK, Notch signaling augments the canonical Wnt pathway to specify the size of the otic placode, Development 135 (13) (2008) 2251–2261. [PubMed: 18495817]

[42]. Ohyama T, Mohamed OA, Taketo MM, Dufort D, Groves AK, Wnt signals mediate a fate decision between otic placode and epidermis, Development 133 (5) (2006) 865–875. [PubMed: 16452098]

[43]. Ma JY, You D, Li WY, Lu XL, Sun S, Li HW, Bone morphogenetic proteins and inner ear development, J. Zhejiang Univ. Sci. B 20 (2) (2019) 131–145. [PubMed: 30112880]

[44]. Tambalo M, Anwar M, Ahmed M, Streit A, Enhancer activation by FGF signalling during otic induction, Dev. Biol 457 (1) (2020) 69–82. [PubMed: 31539539]

[45]. Frenz DA, Liu W, Cvekl A, Xie Q, Wassef L, Quadro L, et al. , Retinoid signaling in inner ear development: A “Goldilocks” phenomenon, Am. J. Med. Genet A 152A (12) (2010) 2947–2961. [PubMed: 21108385]

[46]. Bok J, Raft S, Kong KA, Koo SK, Drager UC, Wu DK, Transient retinoic acid signaling confers anterior-posterior polarity to the inner ear, Proc. Natl. Acad. Sci. USA 108 (1) (2011) 161–166. [PubMed: 21173260]

[47]. Wu DK, Kelley MW, Molecular mechanisms of inner ear development, Cold Spring Harb. Perspect. Biol 4 (8) (2012) a008409. [PubMed: 22855724]

[48]. Shearer AE, Hildebrand MS, Odell AM, Smith RJH, in: Adam MP, Feldman J, Mirzaa GM, Pagon RA, Wallace SE, Amemiya A (Eds.), Genetic Hearing Loss Overview, GeneReviews((R)), Seattle (WA), 1993.

[49]. Acke FR, Dhooge IJ, Malfait F, De Leenheer EM, Hearing impairment in Stickler syndrome: a systematic review, Orphanet J. Rare Dis 7 (2012) 84. [PubMed: 23110709]

[50]. Zhu M, Yang T, Wei S, DeWan AT, Morell RJ, Elfenbein JL, et al. , Mutations in the gamma-actin gene (ACTG1) are associated with dominant progressive deafness (DFNA20/26), Am. J. Hum. Genet 73 (5) (2003) 1082–1091. [PubMed: 13680526]

[51]. Zhang X, Huang CT, Chen J, Pankratz MT, Xi J, Li J, et al. , Pax6 is a human neuroectoderm cell fate determinant, Cell Stem Cell 7 (1) (2010) 90–100. [PubMed: 20621053]

[52]. Britton G, Heemskerk I, Hodge R, Qutub AA, Warmflash A, A novel self-organizing embryonic stem cell system reveals signaling logic underlying the patterning of human ectoderm, Development 146 (20) (2019).

[53]. Hu Q, Ueno N, Behringer RR, Restriction of BMP4 activity domains in the developing neural tube of the mouse embryo, EMBO Rep 5 (7) (2004) 734–739. [PubMed: 15218525]

[54]. Thier MC, Hommerding O, Panten J, Pinna R, Garcia-Gonzalez D, Berger T, et al. , Identification of embryonic neural plate border stem cells and their generation by direct reprogramming from adult human blood cells, Cell Stem Cell 24 (1) (2019) 166–182 e13. [PubMed: 30581079]

[55]. Zeng B, Liu Z, Lu Y, Zhong S, Qin S, Huang L, et al. , The single-cell and spatial transcriptional landscape of human gastrulation and early brain development, Cell Stem Cell 30 (6) (2023) 851–866 e7. [PubMed: 37192616]

[56]. Maier EC, Saxena A, Alsina B, Bronner ME, Whitfield TT, Sensational placodes: neurogenesis in the otic and olfactory systems, Dev. Biol 389 (1) (2014) 50–67. [PubMed: 24508480]

[57]. Kevin Shengyang Yu SMF, Jason S. Park, Katharine Lee, Daniel M. Wong, Lauren Byrnes, Sarah M. Knox, Julie B. Sneddon, Aaron D. Tward. Development of the Mouse and Human Cochlea at Single Cell Resolution. bioRxiv [Preprint]. 2019.

[58]. Hartman BH, Durruthy-Durruthy R, Laske RD, Losorelli S, Heller S, Identification and characterization of mouse otic sensory lineage genes, Front Cell Neurosci 9 (2015) 79. [PubMed: 25852475]

[59]. Miura T, Kouno T, Takano M, Kuroda T, Yamamoto Y, Kusakawa S, et al. , Single-cell RNA-seq reveals LRRC75A-expressing cell population involved in VEGF secretion of multipotent mesenchymal stromal/stem cells under ischemia, Stem Cells Transl. Med 12 (6) (2023) 379–390. [PubMed: 37263619]

[60]. Bohnenpoll T, Trowe MO, Wojahn I, Taketo MM, Petry M, Kispert A, Canonical Wnt signaling regulates the proliferative expansion and differentiation of fibrocytes in the murine inner ear, Dev. Biol 391 (1) (2014) 54–65. [PubMed: 24727668]

[61]. Li C, Wang J, Kong J, Tang J, Wu Y, Xu E, et al. , GDF15 promotes EMT and metastasis in colorectal cancer, Oncotarget 7 (1) (2016) 860–872. [PubMed: 26497212]

[62]. Qin Q, Xu Y, He T, Qin C, Xu J, Normal and disease-related biological functions of Twist1 and underlying molecular mechanisms, Cell Res 22 (1) (2012) 90–106. [PubMed: 21876555]

[63]. Sai X, Ladher RK, Early steps in inner ear development: induction and morphogenesis of the otic placode, Front Pharm 6 (2015) 19.

[64]. Roccio M, Perny M, Ealy M, Widmer HR, Heller S, Senn P, Molecular characterization and prospective isolation of human fetal cochlear hair cell progenitors, Nat. Commun 9 (1) (2018) 4027. [PubMed: 30279445]

[65]. Kolla L, Kelly MC, Mann ZF, Anaya-Rocha A, Ellis K, Lemons A, et al. , Characterization of the development of the mouse cochlear epithelium at the single cell level, Nat. Commun 11 (1) (2020) 2389. [PubMed: 32404924]

[66]. Stone JS, Shang JL, Tomarev S, Expression of Prox1 defines regions of the avian otocyst that give rise to sensory or neural cells, J. Comp. Neurol 460 (4) (2003) 487–502. [PubMed: 12717709]

[67]. Wright TJ, Mansour SL, Fgf3 and Fgf10 are required for mouse otic placode induction, Development 130 (15) (2003) 3379–3390. [PubMed: 12810586]

[68]. Alvarez Y, Alonso MT, Vendrell V, Zelarayan LC, Chamero P, Theil T, et al. , Requirements for FGF3 and FGF10 during inner ear formation, Development 130 (25) (2003) 6329–6338. [PubMed: 14623822]

[69]. Ladher RK, Wright TJ, Moon AM, Mansour SL, Schoenwolf GC, FGF8 initiates inner ear induction in chick and mouse, Genes Dev 19 (5) (2005) 603–613. [PubMed: 15741321]

[70]. Rinkwitz S, Bober E, Baker R, Development of the vertebrate inner ear, Ann. N. Y Acad. Sci 942 (2001) 1–14. [PubMed: 11710453]

[71]. Urness LD, Paxton CN, Wang X, Schoenwolf GC, Mansour SL, FGF signaling regulates otic placode induction and refinement by controlling both ectodermal target genes and hindbrain Wnt8a, Dev. Biol 340 (2) (2010) 595–604. [PubMed: 20171206]

[72]. Durruthy-Durruthy R, Gottlieb A, Hartman BH, Waldhaus J, Laske RD, Altman R, et al. , Reconstruction of the mouse otocyst and early neuroblast lineage at single-cell resolution, Cell 157 (4) (2014) 964–978. [PubMed: 24768691]

[73]. Freter S, Muta Y, Mak SS, Rinkwitz S, Ladher RK, Progressive restriction of otic fate: the role of FGF and Wnt in resolving inner ear potential, Development 135 (20) (2008) 3415–3424. [PubMed: 18799542]

[74]. Wilson PA, Lagna G, Suzuki A, Hemmati-Brivanlou A, Concentration-dependent patterning of the Xenopus ectoderm by BMP4 and its signal transducer Smad1, Development 124 (16) (1997) 3177–3184. [PubMed: 9272958]

[75]. Abello G, Khatri S, Radosevic M, Scotting PJ, Giraldez F, Alsina B, Independent regulation of Sox3 and Lmx1b by FGF and BMP signaling influences the neurogenic and non-neurogenic domains in the chick otic placode, Dev. Biol 339 (1) (2010) 166–178. [PubMed: 20043898]

[76]. Ohta S, Mansour SL, Schoenwolf GC, BMP/SMAD signaling regulates the cell behaviors that drive the initial dorsal-specific regional morphogenesis of the otocyst, Dev. Biol 347 (2) (2010) 369–381. [PubMed: 20837004]

[77]. Bademci G, Abad C, Cengiz FB, Seyhan S, Incesulu A, Guo S, et al. , Long-range cis-regulatory elements controlling GDF6 expression are essential for ear development, J. Clin. Invest 130 (8) (2020) 4213–4217. [PubMed: 32369452]

[78]. Chang W, Nunes FD, De Jesus-Escobar JM, Harland R, Wu DK, Ectopic noggin blocks sensory and nonsensory organ morphogenesis in the chicken inner ear, Dev. Biol 216 (1) (1999) 369–381. [PubMed: 10588886]

[79]. Gerlach LM, Hutson MR, Germiller JA, Nguyen-Luu D, Victor JC, Barald KF, Addition of the BMP4 antagonist, noggin, disrupts avian inner ear development, Development 127 (1) (2000) 45–54. [PubMed: 10654599]

[80]. Gibaja A, Aburto MR, Pulido S, Collado M, Hurle JM, Varela-Nieto I, et al. , TGFbeta2-induced senescence during early inner ear development, Sci. Rep 9 (1) (2019) 5912. [PubMed: 30976015]

[81]. Varghese DS, Parween S, Ardah MT, Emerald BS, Ansari SA, Effects of Aminoglycoside Antibiotics on Human Embryonic Stem Cell Viability during Differentiation In Vitro, Stem Cells Int 2017 (2017) 2451927. [PubMed: 29147115]

[82]. Costigan A, Hollville E, Martin SJ, Discriminating between apoptosis, necrosis, necroptosis, and ferroptosis by microscopy and flow cytometry, Curr. Protoc 3 (12) (2023) e951. [PubMed: 38112058]

[83]. Korzeniewski C, Callewaert DM, An enzyme-release assay for natural cytotoxicity, J. Immunol. Methods 64 (3) (1983) 313–320. [PubMed: 6199426]

[84]. Dehne N, Rauen U, de Groot H, Lautermann J, Involvement of the mitochondrial permeability transition in gentamicin ototoxicity, Hear Res 169 (1–2) (2002) 47–55. [PubMed: 12121739]

[85]. Reed JC, Cytochrome c: can't live with it–can't live without it, Cell 91 (5) (1997) 559–562. [PubMed: 9393848]

[86]. Kim J, Hemachandran S, Cheng AG, Ricci AJ, Identifying targets to prevent aminoglycoside ototoxicity, Mol. Cell Neurosci 120 (2022) 103722. [PubMed: 35341941]

[87]. Kim J, Ricci AJ, In vivo real-time imaging reveals megalin as the aminoglycoside gentamicin transporter into cochlea whose inhibition is otoprotective, Proc. Natl. Acad. Sci. USA 119 (9) (2022).

[88]. Hosokawa S, Hosokawa K, Ishiyama G, Ishiyama A, Lopez IA, Immunohistochemical localization of megalin and cubilin in the human inner ear, Brain Res 1701 (2018) 153–160. [PubMed: 30218661]

[89]. Nieweg K, Andreyeva A, van Stegen B, Tanriöver G, Gottmann K, Alzheimer's disease-related amyloid-β induces synaptotoxicity in human iPS cell-derived neurons, Cell Death Dis 6 (4) (2015) e1709. [PubMed: 25837485]

[90]. Vazin T, Ball KA, Lu H, Park H, Ataeijannati Y, Head-Gordon T, et al. , Efficient derivation of cortical glutamatergic neurons from human pluripotent stem cells: a model system to study neurotoxicity in Alzheimer's disease, Neurobiol. Dis 62 (2014) 62–72. [PubMed: 24055772]

[91]. Gonzalez C, Armijo E, Bravo-Alegria J, Becerra-Calixto A, Mays CE, Soto C, Modeling amyloid beta and tau pathology in human cerebral organoids, Mol. Psychiatry 23 (12) (2018) 2363–2374. [PubMed: 30171212]

[92]. Raja WK, Mungenast AE, Lin YT, Ko T, Abdurrob F, Seo J, et al. , Self-organizing 3D human neural tissue derived from induced pluripotent stem cells recapitulate alzheimer's disease phenotypes, PLoS One 11 (9) (2016) e0161969. [PubMed: 27622770]

[93]. Jensen-Smith HC, Hallworth R, Nichols MG, Gentamicin rapidly inhibits mitochondrial metabolism in high-frequency cochlear outer hair cells, PLoS One 7 (6) (2012) e38471. [PubMed: 22715386]

[94]. Sha SH, Taylor R, Forge A, Schacht J, Differential vulnerability of basal and apical hair cells is based on intrinsic susceptibility to free radicals, Hear Res 155 (1–2) (2001) 1–8. [PubMed: 11335071]

[95]. Chen Q, Mahendrasingam S, Tickle JA, Hackney CM, Furness DN, Fettiplace R, The development, distribution and density of the plasma membrane calcium ATPase 2 calcium pump in rat cochlear hair cells, Eur. J. Neurosci 36 (3) (2012) 2302–2310. [PubMed: 22672315]

[96]. Baker RS, Chole RA, A randomized clinical trial of topical gentamicin after tympanostomy tube placement, Arch. Otolaryngol. Head. Neck Surg 114 (7) (1988) 755–757. [PubMed: 3289583]

[97]. Hussain SZM, Hashmi SS, Qayyum A, Ototoxicity of topical antibiotic ear drops in chronic suppurative otitis media in humans: a review of the literature, Cureus 14 (12) (2022) e32780. [PubMed: 36686080]

[98]. Bath AP, Walsh RM, Bance ML, Rutka JA, Ototoxicity of topical gentamicin preparations, Laryngoscope 109 (7 Pt 1) (1999) 1088–1093. [PubMed: 10401847]

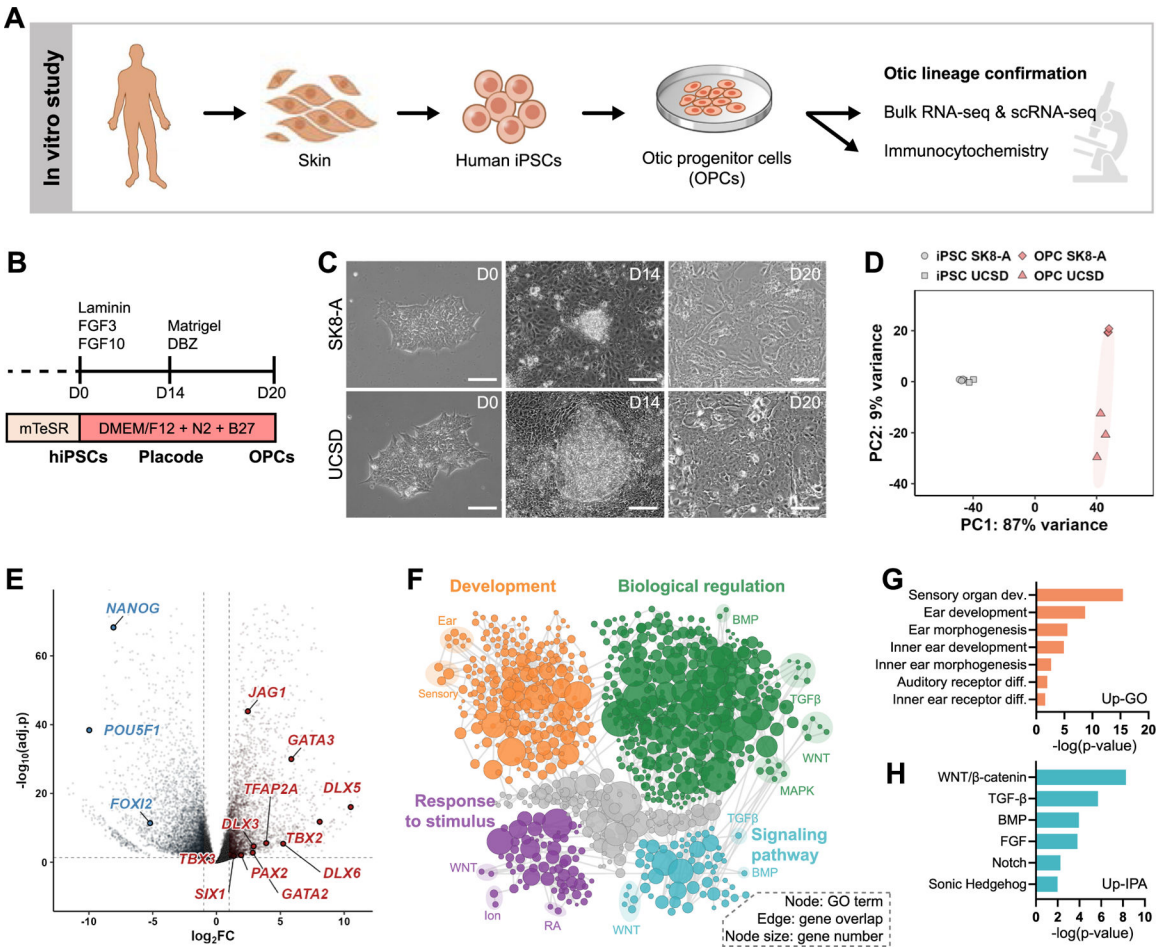

Fig. 1. Derivation of human OPCs from hiPSCs and transcriptomic profiling.

(**A**) Schematic overview of the experimental pipeline, from human skin biopsy to hiPSCs generation, OPC differentiation, and subsequent OPC characterization. (**B**) Schematic representation of the protocol used for OPC differentiation from hiPSCs. (**C**) Representative bright-field images showing hiPSCs (day 0), cells at the placodal stage (day 14), and OPCs (day 20). Scale bars = 100 μm. (**D**) Principal component (PC) analysis plot illustrating the clustering of hiPSCs and OPCs. Each point represents an individual sample. (**E**) Volcano plot depicting differentially expressed genes in OPCs compared to hiPSCs, highlighting the up-regulation of otic lineage markers and down-regulation of pluripotency-related genes. p-adj < 0.05. 3 samples from each SK8-A and UCSD lines were combined for the analysis. (**F**) Gene set enrichment analysis of OPCs (SK8-A and UCSD combined data set) visualized as a network using Cytoscape. (**G**) Gene ontology (GO) analysis highlighting significantly enriched biological processes related to “ear” in OPCs compared to hiPSCs. (**H**) Ingenuity Pathway Analysis (IPA) identifying up-regulated canonical pathways in OPCs. Abbreviations: fibroblast growth factor 3 (FGF3); fibroblast growth factor 10 (FGF10); fold change (FC); dibenzazepine (DBZ); Dulbecco’s Modified Eagle Medium F12 (DMEM/F12); hiPSCs, human induced pluripotent stem cells; scRNA-seq, single-cell RNA sequencing; transforming growth factor beta (TGF-β).

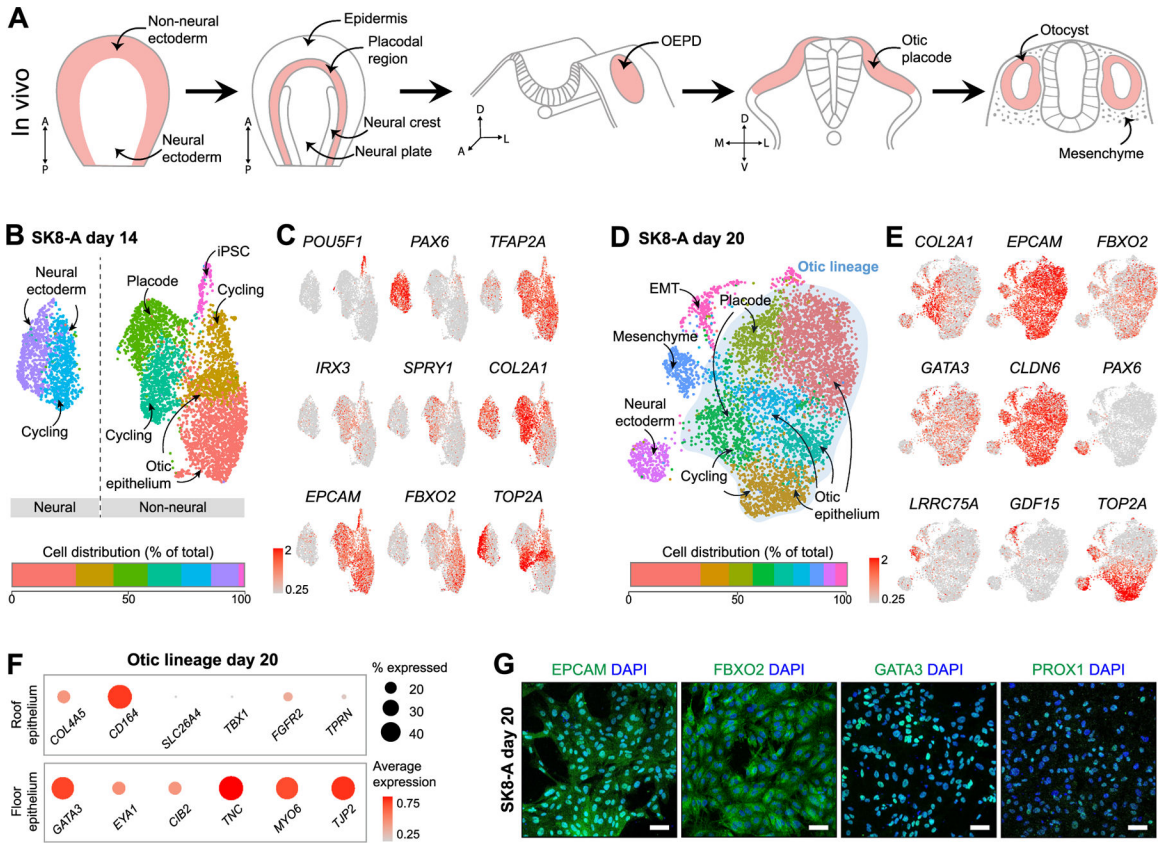

Fig. 2. Characterization of cell types during human OPC differentiation.

(**A**) Schematic illustrations of early inner ear development, with the pink region indicating the origin of the otic lineage. (**B**) UMAP plots of day 14 differentiation with the SK8-A line, alongside the percentage distribution of all identified cell clusters. (**C**) Feature plots displaying key gene markers used to classify cell subtypes and the determination of neural- and non-neural origin cells. (**D**) UMAP plots of day 20 differentiation with the SK8-A line and percentage distribution of all cell clusters. (**E**) Feature plots showing the expression of key gene markers associated with the otic lineage and the surrounding cell population. (**F**) Dot plots illustrating the expression of genes characteristic of the roof epithelium and floor epithelium during human inner ear development [57] in OPCs. (**G**) Protein expression of otic-related markers (green) in OPCs; DAPI (blue) stains nuclei. Scale bar, 50 μm. Abbreviations: iPSC, induced pluripotent stem cell; EMT, epithelial-to-mesenchymal transition; OEPD, otic epibranchial placode,

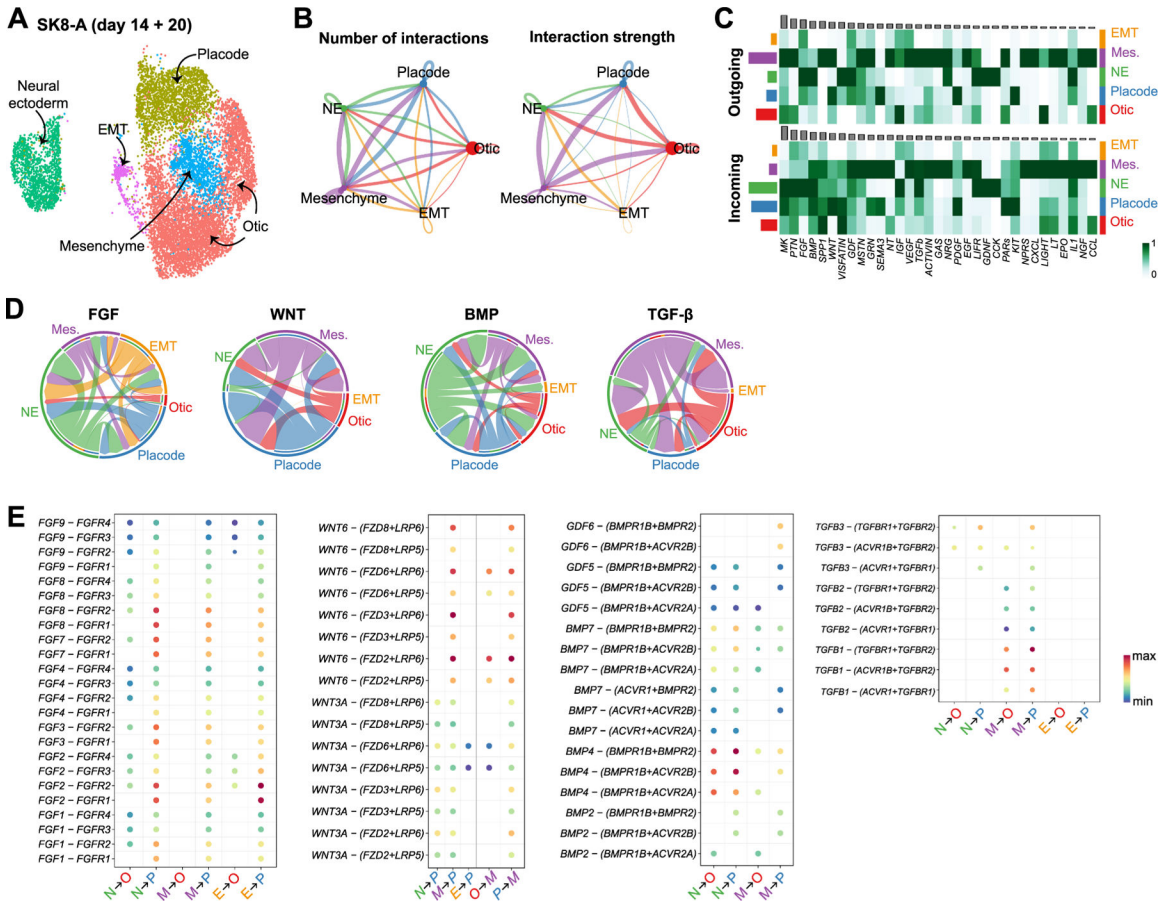

Fig. 3. Cell-cell communication analysis using CellChat.

(**A**) UMAP plot of combined day 14 and day 20 datasets from SK8-A line, with cell type annotations. (**B**) Number of ligand-receptor pairs and interaction strength between any pair of two cell populations. The line width is proportional to the indicated number of ligand-receptor pairs and interaction strength. NE, neural ectoderm. (**C**) Inferred outgoing and incoming signaling pathways. The histograms on the left and top display the contribution of each cell type and signaling pathway to the pattern, respectively. The gray to dark-green color scale indicates relative strength. Mes, mesenchyme. (**D**) Chord diagrams displaying cell-cell interactions in FGF, WNT, BMP, and TGF-β signaling pathways. Arrows indicate the direction of signaling from sender to receiver cell types. (**E**) Ligand-receptor pairs that are related to the FGF, WNT, and BMP signaling pathways, targeting the placode (P), otic (O), or mesenchyme (M) cluster. Dot color represents the calculated communication probability. N, neural ectoderm. E, EMT.

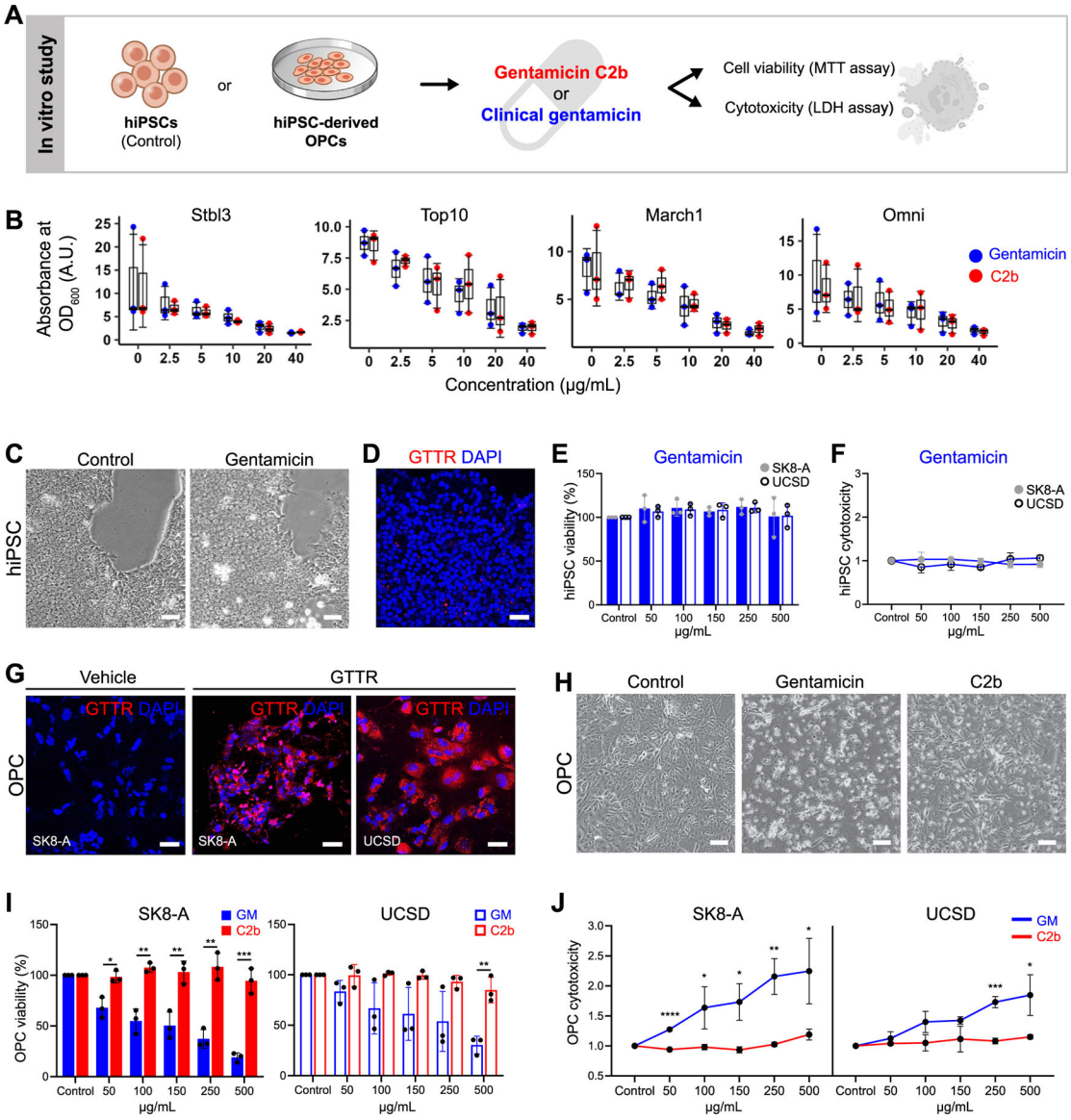

Fig. 4. Evaluation of gentamicin and gentamicin C2b toxicity in hiPSCs and human OPCs.

(**A**) Schematic overview of experimental design testing the toxicity of gentamicin C2b and clinical gentamicin in human in vitro models. (**B**) Box plots show the mean normalized absorbance at OD_{600} (A.U.) across biological replicates, measured after treatment with increasing concentrations of gentamicin or C2b. Error bars represent standard deviation. Individual normalized replicate means are overlaid as points. Data are grouped by E. coli strain (indicated by facet labels), and points are color-coded by treatment: C2b (red) and gentamicin (blue). Statistical differences were assessed using *t*-tests; non-significant differences are not shown. Sample size: n = 3 biological triplicates, each with technical triplicates. (**C**) Representative bright-field images of SK8-A hiPSCs under control conditions and after 24 h exposure to 500 μg/mL clinical gentamicin. Scale bars 50 μm. (**D**) Lack of red fluorescence in hiPSCs after 24 h exposure to Texas Red-conjugated gentamicin GTTR, indicating no gentamicin uptake. Scale bars 50 μm. (**E**, **F**) Assessing cell viability

using MTT assay (**E**) and cytotoxicity using LDH assay (**F**) in hiPSCs exposed to six different concentrations of gentamicin for 24 h. No significant differences were observed across all groups in both hiPSC lines. (**G**) Red fluorescence images showing GTTR uptake in OPCs. Scale bars 50 μm. (**H**) Representative bright-field images of OPCs (SK8-A) under control conditions and after 24 h exposure to 500 μg/mL gentamicin or gentamicin C2b. Scale bars 100 μm. (**I**, **J**) Quantification of cell viability (**I**) and cytotoxicity (**J**) in OPCs exposed to gentamicin (GM) or gentamicin C2b for 24 h. Data are presented as mean ± SD from the combined results of at least 3 independent experiments, each containing 3–4 technical replicates. Unpaired *t*-tests were used to assess statistical differences between gentamicin- and gentamicin C2b-treated groups. *$P < 0.05$; **$P < 0.01$; ***$P < 0.001$; ****$P < 0.0001$.

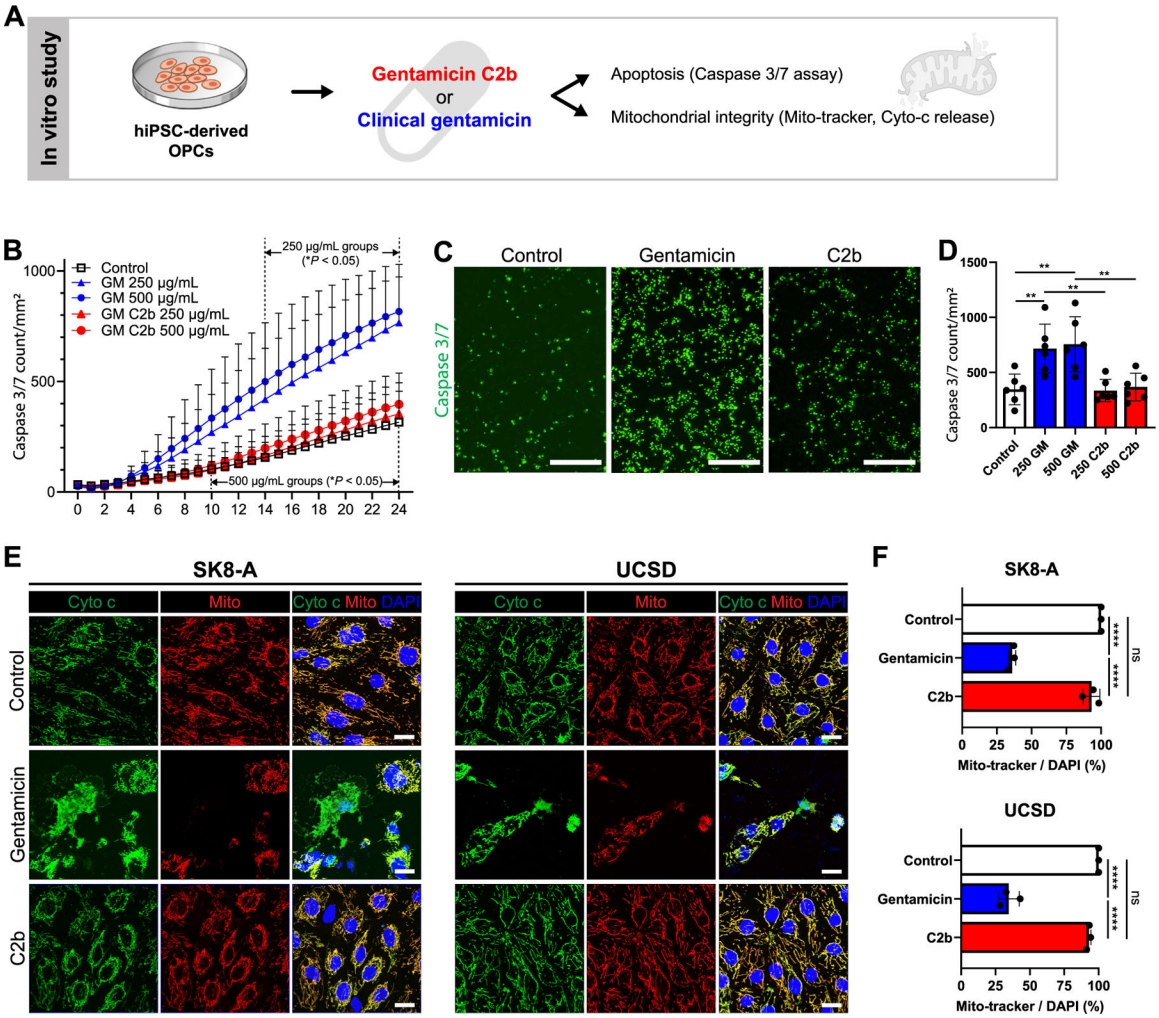

Fig. 5. Effects of gentamicin and gentamicin C2b on the mitochondria of human OPCs.

(**A**) Schematic overview of experimental design testing mitochondrial-dependent apoptosis induced by gentamicin C2b and clinical gentamicin in OPCs. (**B**) Live cell imaging was performed every hour for 24 h using the real-time IncuCyte caspase 3/7 green dye fluorescence assay. OPCs differentiated from SK8-A hiPSCs were treated with 250 µg/mL or 500 µg/mL gentamicin or gentamicin C2b for 24 h. Data are presented as mean ± SD (n ≥ 5). (**C**) Representative images of caspase 3/7 green positive cells after 24 h exposure to vehicle control, 500 µg/mL gentamicin, or 500 µg/mL gentamicin C2b. Scale bars 400 nm. (**D**) Bar graph indicating no significant differences in caspase 3/7 fluorescence between gentamicin C2b-exposed groups and controls at 24 h, as shown in panel B. (**E**) Representative fluorescence images of OPCs stained for cytochrome c (Cyto c; green), Mito-Tracker (Mito; red), and DAPI (blue) following 24 h exposure to 500 µg/mL gentamicin, 500 µg/mL gentamicin C2b, or vehicle control. Scale bars: 20 µm. (**F**) Quantification of active mitochondria based on the percentage of Mito-Tracker positive area, normalized to the number of DAPI-stained nuclei, after 24 h exposure to 500 µg/mL gentamicin, 500 µg/mL gentamicin C2b, or vehicle control. Data are presented as mean ± SD. *$P < 0.05$; **$P < 0.01$; ***$P < 0.001$; ****$P < 0.0001$ in all panels.

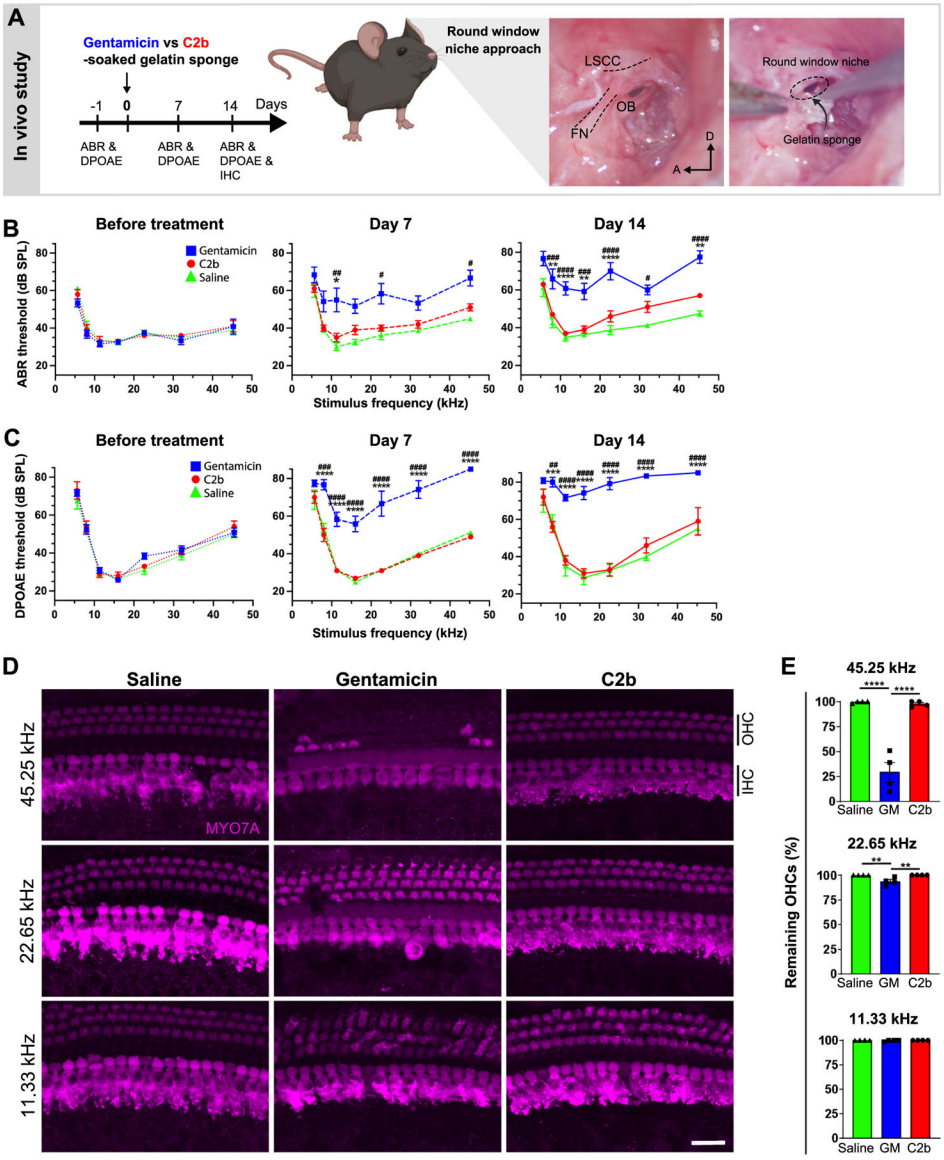

Fig. 6. Evaluation of gentamicin and gentamicin C2b ototoxicity in mice in vivo.

(A). Schematic overview of the in vivo experimental design with representative images of the round window niche surgical approach. The left image shows the round window niche and surrounding anatomical landmarks: otic bulla (OB), facial nerve (FN), lateral semicircular canal (LSCC), dorsal (D), and anterior (A). The right image shows the gelatin sponge being advanced toward the round window niche (dotted circle) during placement. (**B**, **C**) Groups of male CBA/J mice aged 8–10 weeks underwent surgery to place a small piece of gelatin sponge soaked in 200 mg/mL gentamicin, 200 mg/mL gentamicin C2b (C2b), or saline (control) in the round window niche. ABR (**B**) and DPOAE (**C**) thresholds (dB SPL, mean ± SEM) were measured in gentamicin (n = 6), C2b (n = 5), and saline (n = 4) treated groups preoperatively and at 1 and 2 weeks postoperatively. $^{*}P < 0.05$, $^{**/\#\#}P < 0.01$, $^{*}{}^{**/\#\#\#}P < 0.001$, $^{****/\#\#\#\#}P < 0.0001$ (* for gentamicin vs. C2b, # for gentamicin vs. saline). (**D**) Representative cochlear whole mounts stained with MYO7A corresponding to

the 11.33, 22.65, and 45.25 kHz regions of the cochlea from mice exposed to gentamicin, C2b, or saline, sacrificed 2 weeks post-exposure. N = 4 in each group. IHC, inner hair cells. OHC, outer hair cells. Scale bar: 20 μm. (**E**) Quantification of surviving OHCs is presented as a percentage. Data are presented as mean ± SEM. $^{**}P < 0.01$ and $^{****}P < 0.0001$.